



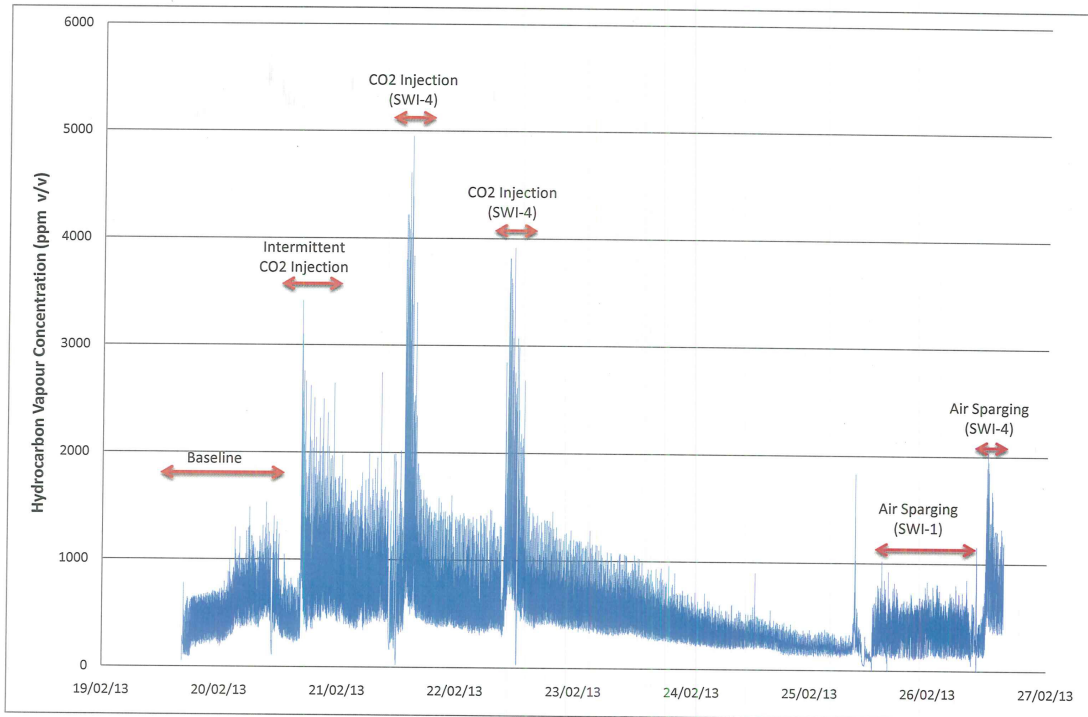
23000 Dyke Road, Unit 21
Richmond, BC V6V 2H3
North CA (415) 390-5483
South CA (714) 924-5483
Canada (604) 562-7836

Carbon Dioxide

Supersaturated Water Injection (SWI) is an effective technology for Nonaqueous Phase Liquid (NAPL) recovery. Carbon dioxide (CO₂) supersaturated water injected into the subsurface results in the nucleation of CO₂ bubbles at and away from the injection point. As the supersaturated liquid flows through the porous medium, gas evolution occurs *in situ* as the system returns to thermodynamic equilibrium. The nucleating bubbles coalesce, rise and volatilize residual NAPL ganglia. SWI offers the following benefits:

- Light NAPL (LNAPL) and Dense NAPL (DNAPL) recovery enhancement system for trapped and immobile NAPL mass
- Uses CO₂ to strip volatile NAPL component for capture in the unsaturated zone
- Mobilizes liquid NAPL trapped in aquifer matrix for recovery

The graph below documents the effectiveness of CO₂ SWI over traditional air sparging.



Please call if you have any questions.

Regards,
John Sankey,
True Blue Technologies

Section 1. Chemical product and company identification

Product name	: Carbon Dioxide
Supplier	: AIRGAS INC., on behalf of its subsidiaries 259 North Radnor-Chester Road Suite 100 Radnor, PA 19087-5283 1-610-687-5253
Product use	: Synthetic/Analytical chemistry.
Synonym	: Carbonic Acid, Carbon Dioxide Liquid, Carbon Dioxide, Refrigerated Liquid, Carbonic Anhydride
MSDS #	: 001013
Date of Preparation/Revision	: 1/20/2012.
In case of emergency	: 1-866-734-3438

Section 2. Hazards identification

Physical state	: Gas or Liquid.
Emergency overview	: WARNING! GAS: CONTENTS UNDER PRESURE. MAY CAUSE RESPIRATORY TRACT, EYE, AND SKIN IRRITATION. CAN CAUSE TARGET ORGAN DAMAGE. Do not puncture or incinerate container. Can cause rapid suffocation. LIQUID: MAY CAUSE RESPIRATORY TRACT, EYE, AND SKIN IRRITATION. CAN CAUSE TARGET ORGAN DAMAGE. Extremely cold liquid and gas under pressure. Can cause rapid suffocation. May cause severe frostbite. Do not puncture or incinerate container. Avoid contact with eyes, skin and clothing. May cause target organ damage, based on animal data. Wash thoroughly after handling. Keep container closed. Avoid breathing gas. Use with adequate ventilation. Contact with rapidly expanding gas, liquid, or solid can cause frostbite.
Target organs	: May cause damage to the following organs: lungs.
Routes of entry	: Inhalation Dermal Eyes
Potential acute health effects	
Eyes	: Moderately irritating to eyes. Contact with rapidly expanding gas may cause burns or frostbite. Contact with cryogenic liquid can cause frostbite and cryogenic burns.
Skin	: Moderately irritating to the skin. Contact with rapidly expanding gas may cause burns or frostbite. Contact with cryogenic liquid can cause frostbite and cryogenic burns.
Inhalation	: Moderately irritating to the respiratory system.
Ingestion	: Ingestion is not a normal route of exposure for gases. Contact with cryogenic liquid can cause frostbite and cryogenic burns.
Potential chronic health effects	
Chronic effects	: May cause target organ damage, based on animal data.
Target organs	: May cause damage to the following organs: lungs.
Medical conditions aggravated by over-exposure	: Pre-existing disorders involving any target organs mentioned in this MSDS as being at risk may be aggravated by over-exposure to this product.

See toxicological information (Section 11)

Section 3. Composition, Information on Ingredients

<u>Name</u>	<u>CAS number</u>	<u>% Volume</u>	<u>Exposure limits</u>
Carbon Dioxide	124-38-9	100	ACGIH TLV (United States, 2/2010). STEL: 54000 mg/m ³ 15 minute(s). STEL: 30000 ppm 15 minute(s). TWA: 9000 mg/m ³ 8 hour(s). TWA: 5000 ppm 8 hour(s). NIOSH REL (United States, 6/2009). STEL: 54000 mg/m ³ 15 minute(s). STEL: 30000 ppm 15 minute(s). TWA: 9000 mg/m ³ 10 hour(s). TWA: 5000 ppm 10 hour(s). OSHA PEL (United States, 6/2010). TWA: 9000 mg/m ³ 8 hour(s). TWA: 5000 ppm 8 hour(s). OSHA PEL 1989 (United States, 3/1989). STEL: 54000 mg/m ³ 15 minute(s). STEL: 30000 ppm 15 minute(s). TWA: 18000 mg/m ³ 8 hour(s). TWA: 10000 ppm 8 hour(s).

Section 4. First aid measures

No action shall be taken involving any personal risk or without suitable training. If it is suspected that fumes are still present, the rescuer should wear an appropriate mask or self-contained breathing apparatus. It may be dangerous to the person providing aid to give mouth-to-mouth resuscitation.

- Eye contact** : Check for and remove any contact lenses. Immediately flush eyes with plenty of water for at least 15 minutes, occasionally lifting the upper and lower eyelids. Get medical attention immediately.
- Skin contact** : In case of contact, immediately flush skin with plenty of water for at least 15 minutes while removing contaminated clothing and shoes. Wash clothing before reuse. Clean shoes thoroughly before reuse. Get medical attention immediately.
- Frostbite** : Try to warm up the frozen tissues and seek medical attention.
- Inhalation** : Move exposed person to fresh air. If not breathing, if breathing is irregular or if respiratory arrest occurs, provide artificial respiration or oxygen by trained personnel. Loosen tight clothing such as a collar, tie, belt or waistband. Get medical attention immediately.
- Ingestion** : As this product is a gas, refer to the inhalation section.

Section 5. Fire-fighting measures

- Flammability of the product** : Non-flammable.
- Products of combustion** : Decomposition products may include the following materials:
carbon dioxide
carbon monoxide
- Fire-fighting media and instructions** : Use an extinguishing agent suitable for the surrounding fire.

Apply water from a safe distance to cool container and protect surrounding area. If involved in fire, shut off flow immediately if it can be done without risk.

Contains gas under pressure. In a fire or if heated, a pressure increase will occur and the container may burst or explode.
- Special protective equipment for fire-fighters** : Fire-fighters should wear appropriate protective equipment and self-contained breathing apparatus (SCBA) with a full face-piece operated in positive pressure mode.

Section 6. Accidental release measures

- Personal precautions** : Immediately contact emergency personnel. Keep unnecessary personnel away. Use suitable protective equipment (section 8). Shut off gas supply if this can be done safely. Isolate area until gas has dispersed.
- Environmental precautions** : Avoid dispersal of spilled material and runoff and contact with soil, waterways, drains and sewers.
- Methods for cleaning up** : Immediately contact emergency personnel. Stop leak if without risk. Note: see section 1 for emergency contact information and section 13 for waste disposal.

Section 7. Handling and storage

- Handling** : Wash thoroughly after handling. High pressure gas. Do not puncture or incinerate container. Use equipment rated for cylinder pressure. Close valve after each use and when empty. Keep container closed. Avoid contact with skin and clothing. Use with adequate ventilation. Avoid contact with eyes. Protect cylinders from physical damage; do not drag, roll, slide, or drop. Use a suitable hand truck for cylinder movement. Never allow any unprotected part of the body to touch uninsulated pipes or vessels that contain cryogenic liquids. Prevent entrapment of liquid in closed systems or piping without pressure relief devices. Some materials may become brittle at low temperatures and will easily fracture.
- Storage** : Cylinders should be stored upright, with valve protection cap in place, and firmly secured to prevent falling or being knocked over. Cylinder temperatures should not exceed 52 °C (125 °F). For additional information concerning storage and handling refer to Compressed Gas Association pamphlets P-1 Safe Handling of Compressed Gases in Containers and P-12 Safe Handling of Cryogenic Liquids available from the Compressed Gas Association, Inc.

Section 8. Exposure controls/personal protection

- Engineering controls** : Use only with adequate ventilation. Use process enclosures, local exhaust ventilation or other engineering controls to keep worker exposure to airborne contaminants below any recommended or statutory limits.
- Personal protection**
- Eyes** : Safety eyewear complying with an approved standard should be used when a risk assessment indicates this is necessary to avoid exposure to liquid splashes, mists or dusts.
When working with cryogenic liquids, wear a full face shield.
- Skin** : Personal protective equipment for the body should be selected based on the task being performed and the risks involved and should be approved by a specialist before handling this product.
- Respiratory** : Use a properly fitted, air-purifying or air-fed respirator complying with an approved standard if a risk assessment indicates this is necessary. Respirator selection must be based on known or anticipated exposure levels, the hazards of the product and the safe working limits of the selected respirator.
The applicable standards are (US) 29 CFR 1910.134 and (Canada) Z94.4-93
- Hands** : Chemical-resistant, impervious gloves complying with an approved standard should be worn at all times when handling chemical products if a risk assessment indicates this is necessary.
Insulated gloves suitable for low temperatures
- Personal protection in case of a large spill** : Self-contained breathing apparatus (SCBA) should be used to avoid inhalation of the product. Full chemical-resistant suit and self-contained breathing apparatus should be worn only by trained and authorized persons.

Product name

Carbon Dioxide

Carbon dioxide

ACGIH TLV (United States, 2/2010).

STEL: 54000 mg/m³ 15 minute(s).

STEL: 30000 ppm 15 minute(s).

TWA: 9000 mg/m³ 8 hour(s).

TWA: 5000 ppm 8 hour(s).

NIOSH REL (United States, 6/2009).

STEL: 54000 mg/m³ 15 minute(s).

STEL: 30000 ppm 15 minute(s).

TWA: 9000 mg/m³ 10 hour(s).

TWA: 5000 ppm 10 hour(s).

OSHA PEL (United States, 6/2010).

TWA: 9000 mg/m³ 8 hour(s).

TWA: 5000 ppm 8 hour(s).

OSHA PEL 1989 (United States, 3/1989).

STEL: 54000 mg/m³ 15 minute(s).

STEL: 30000 ppm 15 minute(s).

TWA: 18000 mg/m³ 8 hour(s).

TWA: 10000 ppm 8 hour(s).

Consult local authorities for acceptable exposure limits.

Section 9. Physical and chemical properties

Molecular weight	: 44.01 g/mole
Molecular formula	: C-O2
Melting/freezing point	: Sublimation temperature: -79°C (-110.2 to °F)
Critical temperature	: 30.9°C (87.6°F)
Vapor pressure	: 830 (psig)
Vapor density	: 1.53 (Air = 1) Liquid Density@BP: Solid density = 97.5 lb/ft3 (1562 kg/m3)
Specific Volume (ft³/lb)	: 8.7719
Gas Density (lb/ft³)	: 0.114

Section 10. Stability and reactivity

Stability and reactivity	: The product is stable.
Hazardous decomposition products	: Under normal conditions of storage and use, hazardous decomposition products should not be produced.
Hazardous polymerization	: Under normal conditions of storage and use, hazardous polymerization will not occur.

Section 11. Toxicological information

Toxicity data

Product/ingredient name	Result	Species	Dose	Exposure
Carbon dioxide	LC50 Inhalation Gas.	Rat	470000 ppm	30 minutes

IDLH	: 40000 ppm
Chronic effects on humans	: May cause damage to the following organs: lungs.
Other toxic effects on humans	: No specific information is available in our database regarding the other toxic effects of this material to humans.
Specific effects	
Carcinogenic effects	: No known significant effects or critical hazards.
Mutagenic effects	: No known significant effects or critical hazards.
Reproduction toxicity	: No known significant effects or critical hazards.

Section 12. Ecological information

Aquatic ecotoxicity

Not available.

Toxicity of the products of biodegradation : not available

Environmental fate : Not available.

Environmental hazards : This product shows a low bioaccumulation potential.

Toxicity to the environment : Not available.

Section 13. Disposal considerations

Product removed from the cylinder must be disposed of in accordance with appropriate Federal, State, local regulation. Return cylinders with residual product to Airgas, Inc. Do not dispose of locally.

Section 14. Transport information

Regulatory information	UN number	Proper shipping name	Class	Packing group	Label	Additional information
DOT Classification	UN1013 UN2187	CARBON DIOXIDE Carbon dioxide, refrigerated liquid	2.2	Not applicable (gas).		Limited quantity Yes. Packaging instruction Passenger aircraft Quantity limitation: 75 kg Cargo aircraft Quantity limitation: 150 kg
TDG Classification	UN1013 UN2187	CARBON DIOXIDE Carbon dioxide, refrigerated liquid	2.2	Not applicable (gas).		Explosive Limit and Limited Quantity Index 0.125 Passenger Carrying Road or Rail Index 75
Mexico Classification	UN1013 UN2187	CARBON DIOXIDE Carbon dioxide, refrigerated liquid	2.2	Not applicable (gas).		-

“Refer to CFR 49 (or authority having jurisdiction) to determine the information required for shipment of the product.”

Section 15. Regulatory information

United States

U.S. Federal regulations : **TSCA 8(a) IUR**: This material is listed or exempted.
United States inventory (TSCA 8b): This material is listed or exempted.
SARA 302/304/311/312 extremely hazardous substances: No products were found.
SARA 302/304 emergency planning and notification: No products were found.
SARA 302/304/311/312 hazardous chemicals: Carbon dioxide
SARA 311/312 MSDS distribution - chemical inventory - hazard identification:
Carbon dioxide: Sudden release of pressure, Immediate (acute) health hazard, Delayed (chronic) health hazard

State regulations

: **Connecticut Carcinogen Reporting**: This material is not listed.
Connecticut Hazardous Material Survey: This material is not listed.
Florida substances: This material is not listed.
Illinois Chemical Safety Act: This material is not listed.
Illinois Toxic Substances Disclosure to Employee Act: This material is not listed.
Louisiana Reporting: This material is not listed.
Louisiana Spill: This material is not listed.
Massachusetts Spill: This material is not listed.
Massachusetts Substances: This material is listed.
Michigan Critical Material: This material is not listed.
Minnesota Hazardous Substances: This material is not listed.
New Jersey Hazardous Substances: This material is listed.
New Jersey Spill: This material is not listed.
New Jersey Toxic Catastrophe Prevention Act: This material is not listed.
New York Acutely Hazardous Substances: This material is not listed.
New York Toxic Chemical Release Reporting: This material is not listed.
Pennsylvania RTK Hazardous Substances: This material is listed.
Rhode Island Hazardous Substances: This material is not listed.

Canada

WHMIS (Canada) : Class A: Compressed gas.
CEPA Toxic substances: This material is listed.
Canadian ARET: This material is not listed.
Canadian NPRI: This material is not listed.
Alberta Designated Substances: This material is not listed.
Ontario Designated Substances: This material is not listed.
Quebec Designated Substances: This material is not listed.

Section 16. Other information

United States

Label requirements

: **GAS**:
CONTENTS UNDER PRESURE.
MAY CAUSE RESPIRATORY TRACT, EYE, AND SKIN IRRITATION.
CAN CAUSE TARGET ORGAN DAMAGE.
Do not puncture or incinerate container.
Can cause rapid suffocation.
LIQUID:
MAY CAUSE RESPIRATORY TRACT, EYE, AND SKIN IRRITATION.
CAN CAUSE TARGET ORGAN DAMAGE.
Extremely cold liquid and gas under pressure.
Can cause rapid suffocation.
May cause severe frostbite.

Canada

Label requirements

: Class A: Compressed gas.

Carbon Dioxide

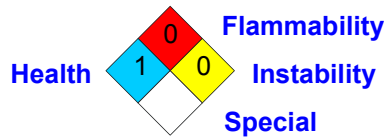
Hazardous Material Information System (U.S.A.) :

Health	*	1
Flammability		0
Physical hazards		0

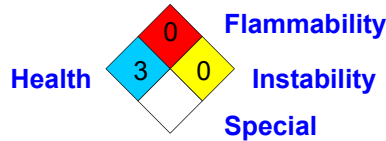
liquid:

Health		3
Fire hazard		0
Reactivity		0
Personal protection		

National Fire Protection Association (U.S.A.) :



liquid:



Notice to reader

To the best of our knowledge, the information contained herein is accurate. However, neither the above-named supplier, nor any of its subsidiaries, assumes any liability whatsoever for the accuracy or completeness of the information contained herein.

Final determination of suitability of any material is the sole responsibility of the user. All materials may present unknown hazards and should be used with caution. Although certain hazards are described herein, we cannot guarantee that these are the only hazards that exist.



Gas exsolution and flow during supersaturated water injection in porous media: II. Column experiments and continuum modeling

R. Enouy^a, M. Li^a, M.A. Ioannidis^{a,*}, A.J.A. Unger^b

^a Department of Chemical Engineering, University of Waterloo, 200 University Ave. W., Waterloo, Ontario, Canada N2L 3G1

^b Department of Earth and Environmental Sciences, University of Waterloo, 200 University Ave. W., Waterloo, Ontario, Canada N2L 3G1

ARTICLE INFO

Article history:

Available online 9 November 2010

Keywords:

Bubble
Mass transfer
Degassing
Percolation
Relative permeability
Ganglion dynamics

ABSTRACT

Degassing and *in situ* development of a mobile gas phase takes place when an aqueous phase equilibrated with a gas at a pressure higher than the subsurface pressure is injected in water-saturated porous media. This process, which has been termed supersaturated water injection (SWI), is a novel and hitherto unexplored means of introducing a gas phase in the subsurface. We give herein a first macroscopic account of the SWI process on the basis of continuum scale simulations and column experiments with CO₂ as the dissolved gas. A published empirical mass transfer correlation [Nambi IM, Powers SE. Mass transfer correlations for nonaqueous phase liquid dissolution from regions with high initial saturations. Water Resour Res 2003;39(2):1030. doi:10.1029/2001WR000667] is found to adequately describe non-equilibrium transfer of CO₂ between the aqueous and gas phases. Remarkably, the dynamics of gas–water two-phase flow, observed in a series of SWI experiments in homogeneous columns packed with silica sand or glass beads, are accurately predicted by traditional two-phase flow theory and the corresponding gas relative permeability is determined. A key consequence of this finding, namely that the displacement of the aqueous phase by gas is compact at the macroscopic scale, is consistent with pore scale simulations of repeated mobilization, fragmentation and coalescence of large gas clusters (i.e., large ganglion dynamics) driven entirely by mass transfer. The significance of this finding for the efficient delivery of a gas phase below the water table is discussed in connection to the alternative process of *in situ* air sparging, and potential advantages of SWI are highlighted.

© 2010 Elsevier Ltd. All rights reserved.

1. Introduction

Gas phase saturation can develop *in situ* within initially water-saturated porous media when injecting an aqueous phase that is equilibrated with gas at a pressure higher than the subsurface pressure. During this process, hereafter referred to as supersaturated water injection (SWI), departure from thermodynamic equilibrium (supersaturation of the aqueous phase) leads to the activation of nucleation sites on the solid surface and the appearance of gas bubbles. Continuing transport of solute mass from the bulk aqueous phase to the gas–liquid interfaces leads to gas phase growth, which at the pore-scale involves the pressurization of bubbles confined in pores by capillary forces and their subsequent expansion into adjacent water-filled pores. A ramified pattern of gas-occupied pores (gas clusters) develops under the influence of capillarity and buoyancy. Gas cluster coalescence during growth, mobilization of sufficiently large clusters under the action of buoyancy, and subsequent fragmentation resulting from capillary instabilities, also contribute

to the complexity of this process, which was studied by pore network simulation in the first part of this contribution [34]. The simulations suggest that a region of finite extent, where gas exsolution takes place, is established with time in the vicinity of the injection point. Mass transfer from the aqueous to the gas phase is confined in this region, the outer boundaries of which are characterized by dissolved gas concentrations near equilibrium with the gas phase. Continuous generation of gas within this region drives immiscible displacement and outward propagation of the gas phase. Pore network simulations [34] indicate that advection of the gas phase takes place via a repeated sequence of gas cluster mobilization, fragmentation and coalescence events governed by the interplay of capillary and buoyancy forces. The two-phase flow regime established at steady state is thus likely one of “large ganglion dynamics” rather than “connected pathway flow” [1,2].

Interest in SWI is motivated by the need to improve the delivery of a gas phase to subsurface environments contaminated by non-aqueous phase liquids (NAPL). Delivery of a gas phase below the water table is needed in bioremediation applications, where oxygen or other reactive gases must be supplied to sustain the destruction of dissolved organic contaminants by micro-organisms [13]. In other instances, involving contaminants occurring as NAPL

* Corresponding author. Tel.: +1 (519) 888 4567x32914; fax: +1 (519) 746 7484.
E-mail address: mioannid@cape.uwaterloo.ca (M.A. Ioannidis).

Nomenclature

p	components: water (w), air (a), and carbon dioxide (CO_2)	P_{cgq}	capillary pressure between aqueous and gas phases [kPa]
l	phases: aqueous (q) and gas (g)	\mathcal{S}_f	super-saturation factor [–]
S_l	saturation of phase l [–]	$\Delta\mathcal{S}_f$	change in super-saturation factor [–]
P_l	pressure of phase l [kPa]	t_0	starting time of SWI experiment [min]
M_l	molar density of phase l [mol/m ³]	t_{SWI}	end time of SWI experiment [min]
X_{pl}	mole fraction of component p in phase l [–]	$t_{\mu\text{-SWI}}$	end time of post-SWI experiment [min]
ρ_l	mass density of phase l [kg/m ³]	$Q_g^{\text{eff}}(t)$	experimental gas phase effluent rate [mL/min]
μ_l	viscosity of phase l [kPa day]	$Q_q^{\text{inj}}(t)$	experimental aqueous phase injection rate [mL/min]
ϕ	porosity of porous media [–]	$Q_q^{\text{eff}}(t)$	experimental aqueous phase effluent rate [mL/min]
\mathbf{K}	intrinsic permeability of porous media [m ²]	$X_{\text{CO}_2q}^{\text{e}}$	equilibrium CO_2 mole fraction in aqueous phase [–]
k_{rl}	relative permeability of phase l [–]	$X_{\text{CO}_2q}^{\text{inj}}$	injected aqueous phase CO_2 mole fraction [–]
D_{pl}	molecular diffusivity of component p in phase l [m ² /day]	σ_{gq}	surface tension between aqueous and gas phase [N/m]
τ	tortuosity of porous media [–]	d_p	particle diameter of porous media [m]
α_L^l	longitudinal dispersivity of phase l [m]	S_g^{nuc}	minimum gas saturation to represent nucleation [–]
α_T^l	transverse dispersivity of phase l [m]	$\beta_0, \beta_1, \beta_{2g}, \beta_{2q}, \beta_3, \beta_4$	non-equilibrium (kinetic) mass transfer coefficients [–]
Q_p	simulated source (+ve) or sink (–ve) term for component p [mol/(m ³ day)]	P^{ref}	reference pressure [kPa]
Bo	Bond number [–]	T^{ref}	reference temperature [K]
g	gravitational acceleration [m/s ²]	a_{wgq}	equilibrium partitioning of water between gas and aqueous phases [kPa]
$\Delta\bar{S}_g$	change in column-averaged gas saturation [–]	a_{CO_2gq}	equilibrium partitioning of CO_2 between gas and aqueous phases [kPa]
$J(S_q)$	Leverett J-function [–]		
k_{rl}	relative permeability of phase l [–]		
n_l	relative permeability exponent of phase l [–]		
S_{lr}	irreducible saturation of phase l [–]		

ganglia trapped below the water table, volatilization into a flowing gas phase may be an effective remedial strategy [21,24]. To achieve these goals, *in situ* air sparging (IAS) has been used to date with varying success [3]. Mass transport effectiveness obviously depends on the spatial distribution of air that can be achieved by IAS within a saturated aquifer and, for this reason, a large number of studies have sought to observe and explain the patterns of gas flow during gas injection [4,6,9,14,16,17,26–29]. At the pore scale, variations in air entry pressure due to ubiquitous random disorder of the pore structure govern the migration of the injected air. Buoyancy and a highly unfavorable viscosity ratio both have a destabilizing effect on the displacement front with the result that, over a broad range of practical conditions, migration of air away from the injection point occurs in the form of separate continuous channels. This picture cannot be accommodated by continuum models of multiphase flow [4,14,26,29] which are consequently limited in their ability to predict air sparging performance in terms of mass transfer.

Bypassing of large portions of the target remediation area due to channeling of the injected air can greatly compromise the remediation effectiveness of IAS. For SWI, on the other hand, one might expect the gas saturation distribution to be relatively insensitive to random disorder of pore size and permeability, at least within the region where gas exsolution takes place. Such an expectation arises from the fact that nucleation can take place in pores of all sizes and the necessary condition for gas cluster growth is transfer of solute mass from the flowing aqueous phase. Gas cluster growth is initially more rapid in areas where the aqueous phase flow velocity is greater, that is in more permeable regions within the porous medium. At the same time, an increase of the gas saturation causes reduction of the effective permeability of these areas. Thus, a greater amount of the injected aqueous phase is diverted to less permeable areas, where gas saturation can also develop, as long as the flowing aqueous phase contains sufficient amount of dissolved gas for activation of nucleation sites and sustained mass transfer.

Beyond the region where gas exsolution takes place, increasing gas saturation is the result of immiscible displacement. At this scale, gas phase mobility is difficult to ascertain by pore network modeling [34] and a macroscopic (continuum) description of SWI becomes necessary.

The objective of this paper is to quantify the dynamics of gas exsolution and flow observed in long columns, packed with silica sand or glass beads, under different conditions (grain size, flow rate and dissolved gas concentration of the injected aqueous phase) of SWI with CO_2 as the dissolved gas. The experimental observations are interpreted using a multiphase, compositional continuum model (CompFlow-SWI) subject to two hypotheses. The first hypothesis is that non-equilibrium mass transfer of CO_2 between the aqueous and gas phases can be described by the correlation of Nambi and Powers [23], slightly modified to capture nucleation within the context of continuum modeling. This hypothesis logically follows from pore network simulation results [34]. A second hypothesis is that gas advection is stabilized by mass transfer, such that displacement of the aqueous phase by gas is compact at the macroscopic scale and can, therefore, be described in a continuum sense using relative permeability concepts. Specifically, we test whether the advection of the leading edge of the gas phase at a critical saturation is consistent with experimental data. The paper is structured as follows. The experimental setup and procedures are first introduced. The parameters and equations used by the continuum-scale simulation software, CompFlow-SWI, are detailed in a subsequent section. These include the relative permeability, capillary pressure and mass transfer data and models adopted for describing this system. The Results and Discussion Section compares experimental results with simulation to validate the mass transfer and gas phase relative permeability models chosen. Upon validation, the simulation is used to determine the effects of nucleation, and a relationship between changes in supersaturation and gas phase nucleation is observed. Key findings and implications for future research are summarized in Section 5.

2. Experimental methods

A series of laboratory experiments were conducted in which an aqueous phase supersaturated with CO₂ was injected at the bottom of a vertically-oriented packed column that was initially saturated with degassed water. By supersaturated, we mean that the concentration of CO₂ in the injected aqueous phase is greater than its solubility in water at the column pressure. In order to achieve a supersaturated aqueous phase, tap water and CO₂ gas from a pressurized cylinder were continuously supplied to a hollow-fiber membrane contactor (InVentures Technologies), operating at a pressure of ca. 5 atm.

Fig. 1 depicts the experimental setup. The Plexiglas column, which is 155 cm long and has an internal diameter of 76 mm, was packed with silica sand or glass beads as follows. A known volume of degassed water was initially added to the column, such that sufficient space for adding the solid particles was available. Solids were continuously added and wet-packed under vibration to prevent the capture of gas bubbles and to reduce the possibility of layering. Some layering was occasionally observed during this procedure and mechanical mixing was also used to achieve packing homogeneity. To prevent the loss of solid particles, fine screens were placed at the top and bottom of the column, supported by springs as necessary. Plates were bolted to the top and bottom of the column to create a closed system, with an injection port at the base and sampling ports throughout the length and at the top of the column. The porosity of the packing was determined from packing dimensions and the volume of water displaced by the solid particles added. Finally, the absolute permeability of the packing was determined by measuring the water flow rate under a fixed pressure gradient. Table 1 summarizes the porous media properties for nine key experiments forming the basis of this work. The ratio of buoyant to capillary forces in these systems is also quantified in Table 1 in terms of the Bond number, defined as follows:

$$Bo = \frac{(\rho_q - \rho_g)gK}{\sigma_{gq}} \quad (1)$$

where ρ_q and ρ_g are the mass density of the aqueous and gas phases, g is gravitational acceleration, K is the absolute permeabil-

ity of the system, and σ_{gq} is the interfacial tension between the gas and aqueous phases. Table 2 lists all the experimental component and phase property data used in the continuum simulations as described in Section 3.

Aqueous and gas phase effluent from the column were sent to a separator. The mass of aqueous phase effluent was collected in a beaker and measured continuously using a digital balance interfaced with a computer. Also interfaced with a computer were a mass flow meter (Omega, model FMA3304), used to measure the gas phase effluent rate which consisted of pure CO₂, and a pressure transducer (Validyne, model DP10-44) used to monitor the aqueous phase pressure at the base of the column. Aqueous phase samples were drawn from sampling ports at distances of 75 cm and 145 cm from the column base to determine the concentration of dissolved CO₂.

At the start of each experiment the column was either freshly packed and, therefore, completely saturated with degassed water, or flushed with copious amounts (~100 PV) of degassed water to ensure that no gas phase (consisting of carbon dioxide with some water vapor) from a previous experiment remained entrapped in the porous media. To conduct an experiment, the valve at the bottom was opened at time t_0 and CO₂-supersaturated water was allowed to flow through the column at constant rate until time t_{SWI} , a period of time sufficiently long for the aqueous phase effluent rate to reach a constant steady-state value. At steady-state, the rate of accumulation of gas within the column was zero and a measurement of the aqueous phase effluent rate provided the flow rate of the injected aqueous phase, Q_q^{inj} . The mole fraction of dissolved CO₂ in the injected aqueous phase, $X_{CO_2,q}^{inj}$, was also determined experimentally as follows. Aqueous phase effluent was first drawn from the top sampling port following establishment of a steady aqueous effluent rate. The effluent sample was immediately added to a sodium hydroxide solution of pH greater than 11. The sodium hydroxide was in excess to ensure that all dissolved CO₂ was converted into disodium carbonate. This mixture was then titrated with hydrochloric acid using phenolphthalein as the titration indicator. Initially the solution was translucent, but changed color as the pH was reduced to 11. The titration was complete when the pH dropped below 9 and the solution became translucent once again. At this point, all of the disodium carbonate was converted

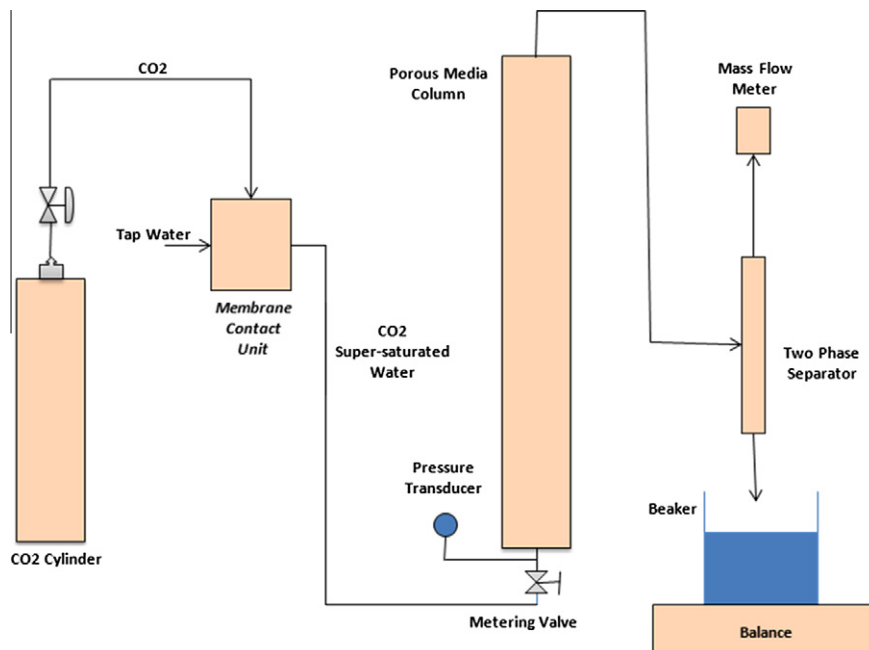


Fig. 1. Experimental setup.

Table 1
Properties of packed columns used in CO₂-SWI experiments.

Experiment ID	Packing	Permeability K (m ²)	Average particle size d_p (μm)	Porosity ϕ (-)	Bo (-)
1	Sand	1.12×10^{-11}	169	0.367	1.52×10^{-6}
2	Sand	1.12×10^{-11}	169	0.367	1.52×10^{-6}
3	Sand	2.91×10^{-11}	305	0.350	3.96×10^{-6}
4	Sand	4.05×10^{-11}	324	0.351	5.51×10^{-6}
5	Sand	3.82×10^{-11}	324	0.352	5.20×10^{-6}
6	Sand	3.82×10^{-11}	324	0.352	5.20×10^{-6}
7	Glass beads	5.65×10^{-11}	254	0.384	7.68×10^{-6}
8	Glass beads	5.65×10^{-11}	254	0.384	7.68×10^{-6}
9	Glass beads	5.65×10^{-11}	254	0.384	7.68×10^{-6}

Table 2
Component and phase property data (at 20 °C).

Property	Value
<i>Compressibility</i>	
\hat{C}_q (kPa ⁻¹)	3.0×10^{-6}
<i>Standard component densities</i>	
M_w^* (mol/m ³)	5.5×10^4
M_a^* (mol/m ³)	41.1
$M_{CO_2}^*$ (mol/m ³)	41.1
<i>Molecular weights</i>	
ω_w (kg/mol)	18.02×10^{-3}
ω_a (kg/mol)	28.97×10^{-3}
ω_{CO_2} (kg/mol)	16.0×10^{-3}
<i>Reference pressure and temperature</i>	
P^{ref} (kPa)	100.0
T^{ref} (K)	298.0
<i>Viscosities</i>	
μ_q (kPa day)	2.44×10^{-11}
μ_g (kPa day)	1.62×10^{-13}
<i>Molecular diffusion coefficient</i>	
$D_{wq} = D_{CO_2q}$ (m ² /day)	3.14×10^{-6}
$D_{wg} = D_{ag} = D_{CO_2g}$ (m ² /day)	1.70×10^{-6}
<i>Molar density</i>	
$M_q = \frac{1 + \hat{C}_q(P_q - P^{ref})}{\sum_p \max(0, X_{pq})/M_p}$, $M_g = \frac{P_g}{RT}$	
<i>Mass density</i>	
$\rho_l = \sum_p X_{pl}\omega_p$	
<i>Equilibrium partitioning coefficients</i>	
a_{wga} (kPa)	11.96
a_{CO_2ga} (kPa)	1.651×10^5
<i>Interfacial tension between gas and aqueous phase</i>	
σ_{gq} (N/m)	72×10^{-3}

into sodium bicarbonate and a mole balance was used to determine the original amount and, hence, the mole fraction of CO₂ in the aqueous effluent. The mole fraction of carbon dioxide in the injected aqueous phase, $X_{CO_2q}^{inj}$, was then determined from a steady-state mass balance of CO₂ over the entire column using the experimentally measured aqueous and gas phase effluent rates, Q_q^{eff} and Q_g^{eff} . The values of Q_q^{inj} and $X_{CO_2q}^{inj}$ for each experiment are listed in Table 3 and are determined from steady-state values of Q_q^{eff} and Q_g^{eff} . It is should be noted that the aqueous phase flow rates realized in the experiments correspond to values of the capillary number, $Ca = \mu_q V_q / \sigma_{gq}$, equal to 1.3×10^{-6} or less.

In each experiment, SWI was stopped at time t_{SWI} and the column response was monitored over time until steady-state was

Table 3
Experimental control variables and measurements.

Experiment ID	Control variables		Measurements		
	Q_q^{inj} (mL/min)	$X_{CO_2q}^{inj}$ (-)	$P_q(t_{SWI})$ (kPa)	$P_q(t_{f-SWI})$ (kPa)	$Q_g^{eff}(t_{SWI})$ (mL/min)
1	27.60	0.002902	188.5	118.6	87.23
2	28.15	0.002599	188.5	118.6	76.14
3	13.20	0.002076	131.7	118.6	26.20
4	20.82	0.002099	133.8	118.6	44.28
5	11.49	0.001798	128.7	118.6	20.16
6	17.40	0.002111	135.8	118.6	37.76
7	18.72	0.001992	128.7	118.6	37.13
8	29.66	0.002005	135.8	118.6	58.16
9	27.60	0.001804	126.7	118.6	20.02

again reached. Experimental data from the two transient periods, one following SWI commencement and the other following SWI termination, are particularly interesting because they are sensitive indicators of the ability of the continuum model to account for the nucleation aspects of the SWI process. In subsequent sections, these data are discussed separately.

3. Numerical model

Presentation of the numerical model in this section focuses on the idea of using a continuum-based multi-phase compositional approach to parameterize two processes that we hypothesize are central to the description of SWI in porous media. The first process is non-equilibrium (kinetic) transfer of CO₂ mass between the gas and aqueous phases. We remind the reader that a multi-phase compositional continuum approach does not simulate the genesis and fate of the gas phase at the pore scale in terms of individual bubbles or distinct clusters of gas-occupied pores, but rather in terms of local gas saturation representing an average over a macroscopic volume of porous media involving a multitude of pores. For a continuum approach to be valid, existence of a representative elementary volume (REV) for gas saturation is a necessary condition. On the basis of experimental data pertaining to the dissolution of residual NAPL in granular media, Nambi and Powers [23] have developed a mass transfer correlation that is valid over a broad range of non-wetting phase saturations. Pore network simulations detailed in the first part of this work [34] suggest that the Nambi and Powers [23] correlation might be used to describe CO₂ mass transfer between the gas and aqueous phases during SWI. Even so, this mass transfer correlation does not describe the kinetics of the initial stage of gas phase formation (nucleation) [18]. During the transient period accompanying SWI commencement, sensitivity of the rate of gas saturation growth to the nucleation characteristics of porous media is also exhibited by pore network simulations [34]. In lieu of a continuum description of heterogeneous nucleation, we propose and test here an *ad hoc* modification to the empirical mass transfer correlation [23], in order to account for the rapid increase of gas saturation at very low levels of gas phase saturation. The second process central to the description of SWI in porous media involves gas-liquid two-phase flow at the continuum scale, where sustained gas flow is the result of mass transfer from an injected aqueous phase rather than the result of direct gas injection. In the context of a continuum-level description, we hypothesize that gas phase mobility can be quantified in terms of a saturation-dependent gas relative permeability function and that the multiphase extension of Darcy's law suffices to describe the advective gas flux. A well-known consequence of this hypothesis for one-dimensional displacement in homogeneous porous media is advection of the gas phase as a "shock front", with the rate of advection of this front controlled by the relative

permeability of the gas phase at a characteristic value of gas phase saturation (greater than the residual gas phase saturation) in a manner analogous to that predicted by the Buckley–Leverett equation [5]. It is a key objective of this paper to test whether this hypothesis conforms to experimental observations.

3.1. Formulation

Formulation of the numerical model CompFlow-SWI largely follows that of Forsyth [10]. However, we restrict the description of the numerical model to focus only on those processes relevant to simulating the SWI experiments described here. Specifically, CompFlow-SWI is a continuum-scale multi-phase, multi-component compositional model that (in the context of this work) considers two mobile phases; namely the aqueous (q), and gas (g) phases. The components considered are water (w), air (a), and carbon dioxide (CO_2). The conservation of moles of component p can be written as:

water: $p = \{w\}$

$$\frac{\partial}{\partial t} \sum_{l=q,g} \phi S_l M_l X_{wl} = - \sum_{l=q,g} \nabla \cdot (M_l X_{wl} \mathbf{V}_l) + \sum_{l=q,g} \nabla \cdot (\phi S_l \mathbf{D}_l M_l \nabla X_{wl}) + Q_w \quad (2)$$

air: $p = \{a\}$

$$\frac{\partial}{\partial t} (\phi S_g M_g X_{ag}) = - \nabla \cdot (M_g X_{ag} \mathbf{V}_g) + \nabla \cdot (\phi S_g \mathbf{D}_g M_g \nabla X_{ag}) + Q_a \quad (3)$$

carbon dioxide: $p = \{\text{CO}_2\}$

$$\begin{aligned} \frac{\partial}{\partial t} (\phi S_q M_q X_{\text{CO}_2q}) &= - \nabla \cdot (M_q X_{\text{CO}_2q} \mathbf{V}_q) \\ &\quad + \nabla \cdot (\phi S_q \mathbf{D}_q M_q \nabla X_{\text{CO}_2q}) + \dot{R}_{\text{CO}_2} + Q_{\text{CO}_2} \\ \frac{\partial}{\partial t} (\phi S_g M_g X_{\text{CO}_2g}) &= - \nabla \cdot (M_g X_{\text{CO}_2g} \mathbf{V}_g) \\ &\quad + \nabla \cdot (\phi S_g \mathbf{D}_g M_g \nabla X_{\text{CO}_2g}) - \dot{R}_{\text{CO}_2} \end{aligned} \quad (4)$$

where Q_p is the rate at which component p is injected/removed (+ve/-ve).

In Eq. (4), \dot{R}_{CO_2} represents the non-equilibrium (kinetic) partitioning rate for the transfer of carbon dioxide from the aqueous to the gas phase, and is given by:

$$\dot{R}_{\text{CO}_2} = S_q^{\beta_{2,q}} M_q \kappa_{\text{CO}_2} (X_{\text{CO}_2q}^* - X_{\text{CO}_2g}) \quad (5)$$

where $X_{\text{CO}_2q}^*$ is the mole fraction of carbon dioxide in the aqueous phase in equilibrium with the gas phase. The rate coefficient κ_{CO_2} is adapted from Nambi and Powers [23] and Unger et al. [32] as:

$$\kappa_{\text{CO}_2} = \beta_0 \left[\max(S_g, S_g^{\text{nuc}}) \right]^{\beta_{2,g}} (\beta_3 + R_q^{\beta_4}) \phi^{\beta_4} \frac{D_{\text{CO}_2q}}{d_p^2} \quad (6)$$

where a *small* gas saturation, S_g^{nuc} , is here introduced *ad hoc* to prevent the computation of unrealistically small mass transfer rates during the initial stages of gas phase formation when $S_g < S_g^{\text{nuc}}$, $R_q = |v_q| \rho_q d_q / \mu_q$ is the aqueous phase Reynolds number, $|v_q|$ is the magnitude of the interstitial aqueous phase velocity and ρ_q is the mass density of the aqueous phase. The various parameters entering Eq. (6) are summarized in Table 4.

The Darcy flux of each phase l is given by:

$$\mathbf{V}_l = -\mathbf{K} \cdot \frac{k_{rl}}{\mu_l} \nabla (P_l + \rho_l g z) \quad (7)$$

Table 4
Simulation parameters and their origin.

Property	Value	Source
<i>Aqueous phase relative permeability in glass beads</i>		
S_{qr} (-)	0.085	[15]
n_q (-)	2.21	[15]
<i>Aqueous phase relative permeability in sand</i>		
S_{qr} (-)	0.20	[20]
n_q (-)	2.89	[20]
<i>Gas phase relative permeability in sand and glass beads</i>		
S_{gr} (-)	0.12	This study
n_g (-)	1.50	This study
<i>Mass transfer rate parameters</i>		
S_g^{nuc} (-)	0.03	This study
β_0 (-)	37.2	[23]
β_1 (-)	0.61	[23]
β_{2g} (-)	1.24	[23]
β_{2q} (-)	0.00	[23]
β_3 (-)	0.01	[32]
β_4 (-)	1.00	[23]

and the dispersion/diffusion tensors have the form:

$$\phi S_l \mathbf{D}_l = \alpha_L^l |\mathbf{V}_l| + \phi S_l \tau D_{pl} \mathbf{I} \quad (8)$$

There exist the following constraints among the above variables:

$$\begin{aligned} S_q + S_g &= 1 \\ X_{wq} + X_{\text{CO}_2q} &= 1 \quad \text{and} \quad X_{wg} + X_{ag} + X_{\text{CO}_2g} = 1 \\ P_g &= P_q + P_{cgq} \end{aligned} \quad (9)$$

where P_{cgq} is the capillary pressure between the gas and aqueous phases.

Equilibrium partitioning of components between the aqueous and gas phases occurs according to the following relationships:

$$\begin{aligned} X_{wg} &= \frac{a_{wga}}{P_g} X_{wq} \\ X_{\text{CO}_2g} &= \frac{a_{\text{CO}_2gq}}{P_g} X_{\text{CO}_2q} \end{aligned} \quad (10)$$

with the air component being insoluble in water $X_{aq} = 0$. This assumption follows from Ref. [10] and allows the gas phase to be present to at least some minimal saturation $S_g^{\text{min}} = 10^{-3} \ll S_g^{\text{nuc}}$. In Ref. [11], Forsyth discusses the theory, implementation and response of the Newton–Raphson iteration to a system of equations aligned with primary and secondary variables (where numerical derivatives are constructed using primary variable switching) in which the gas, aqueous and non-aqueous liquid phases are all allowed to disappear or alternatively appear. In [10], Forsyth demonstrates for a gas venting problem focused on NAPL remediation, forcing the air component to be insoluble in water in order to ensure that gas phase is always present at S_g^{min} yields superior convergence of the Newton–Raphson iteration with near-identical results to within convergence tolerance ($\text{ctol}[P_l] = 10^{-2}$ kPa; $\text{ctol}[S_l] = 10^{-5}$; $\text{ctol}[X_{pl}] = 10^{-7}$), albeit with simulation results perturbed by having the gas phase present at S_g^{min} below the water table in regions distant from active gas venting. In the context of this study, we found values of S_g^{min} in the range of $10^{-5} < S_g^{\text{min}} < 10^{-3}$ yielded identical results in the region of active gas nucleation and advection, with smaller values requiring more Newton–Raphson iterations. This last point is especially true given that $S_g^{\text{min}} \ll S_g^{\text{nuc}}$. Ahead of the region of active gas nucleation and advection, gas saturations of S_g^{min} may physically represent very small gas bubbles trapped by capillary forces in the crevices of sand grains, where these bubbles originate during emplacement of the porous media in the column. In real aquifers, they may originate from microbial activity. Phase and component properties pertinent to the

experiments described in this work are itemized in Table 2. On the basis of literature values [19], a longitudinal dispersivity $\alpha_L^i = 0.1$ m was considered representative of all packs in this work. In contrast, $\alpha_L^g = 0$ given that no values were found in the literature.

Boundary conditions are enforced through the use of the Q_p term. With regards to the experimental column shown on Fig. 1, two specific variations of Q_p are implemented. At the base of the column, the components water and CO_2 are injected using the data listed in Table 3. For instance:

$$\begin{aligned} Q_w &= Q_q^{inj} M_w^* / V_i \\ Q_{\text{CO}_2} &= Q_w X_{\text{CO}_2, q}^{inj} \end{aligned} \quad (11)$$

where V_i is the volume of the node at the base of the column in which Q_w and Q_{CO_2} are injected. At the top of the column, both the aqueous and gas phases exit the column into a reservoir containing water to a depth of 0.1 m. Consequently, the pressure at the top of the column is $P_{BC} = P^{\text{ref}} + 1$ kPa. Let $P_{l,i}$ denote the pressure of phase l in the porous media at the top of the column, within node i . The source/sink term for component p in phase l at the top of the column within node i is given as:

$$\begin{aligned} Q_p &= \sum_{l=q,g} \gamma_{BC,i} \frac{M_{l,i} k_{rl,i}}{\mu_{l,i}} (P_{BC} - P_{l,i}) X_{p,l,i} \quad \text{if } P_{BC} > P_{l,i} \\ Q_w &= \gamma_{BC,i} \frac{M_w^*}{\mu_q} (P_{BC} - P_{q,i}) \quad \text{if } P_{BC} < P_{q,i} \end{aligned} \quad (12)$$

Note that while aqueous and gas phase can exit the top of the column, only aqueous phase consisting of pure water can flow into the top of the column. The parameter $\gamma_{BC,i}$ is an influence coefficient controlling the interaction between the prescribed boundary condition and node i at the top of the column, where both the boundary condition and node i are at the same elevation.

The temporal derivatives of in Eqs. (2) and (4) are discretized using finite differences with fully-implicit time weighting. A finite volume discretization in one-, two- or three-dimensions is used to handle the spatial derivatives. Details of the discretization can be found elsewhere [10,12] and will not be repeated here. All of the component equations are fully-coupled and full Newton–Raphson iteration is used for linearization. This yields a large sparse Jacobian matrix which is subsequently solved using ILU factorization and either CGSTAB or GMRES acceleration [8,25,33].

3.2. Capillary pressure and relative permeability

Aqueous-gas phase capillary pressure data, P_{cgq} , for drainage in unconsolidated packs of glass beads and silica sand were taken from the experimental studies of Ioannidis et al. [15] and Leverett [20] respectively, and are plotted in Fig. 2 in terms of the Leverett J-function $J(S_q)$:

$$J(S_q) = \frac{P_{cgq} \left(\frac{K}{\phi} \right)^{0.5}}{\sigma_{gq}} \quad (13)$$

Aqueous k_{rq} and gas k_{rg} phase relative permeability data for both the sand and glass bead packs were represented as follows [7]:

$$\begin{aligned} k_{rq} &= \left(\frac{S_q - S_{qr}}{1 - S_{qr}} \right)^{n_q} \\ k_{rg} &= \left(\frac{S_g - S_{gr}}{1 - S_{gr}} \right)^{n_g} \end{aligned} \quad (14)$$

where S_{qr} and S_{gr} are the residual aqueous and gas phase saturations, respectively. The gas phase relative permeability parameters S_{gr} and n_g were estimated in this study. Conversely, the aqueous phase relative permeability parameters S_{qr} and n_q for packs of sand and glass beads were taken from the experimental works of Lever-

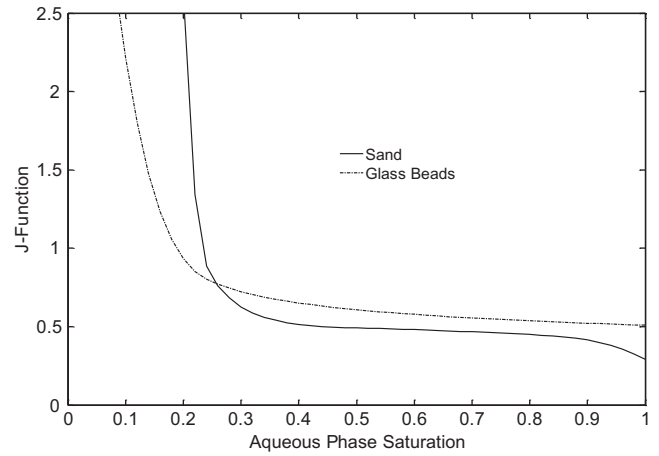


Fig. 2. Leverett J-function for air-water drainage in homogeneous packs of sand or glass beads.

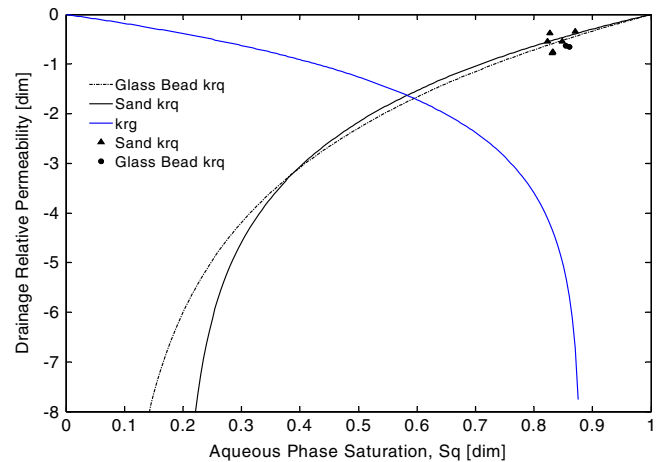


Fig. 3. Simulated aqueous and gas phase relative permeability curves for experiment 8. Experimental steady state aqueous phase relative permeability values for glass bead (circles) and sand pack (triangles) were computed by using the multi-phase extension of the Darcy equation as: $k_{rq}(S_q) = (Q_q^{inj} \mu_q L) / (K A \Delta I_q)$ where L is the column length, A is its cross-sectional area, $\Delta I_q = P_q(t_{SWI}) - P^{\text{ref}} - \rho_q g L$, and $S_q = 1 - \Delta S_g(t_{SWI})$.

ett [20] and Ioannidis et al. [15], respectively. In doing so, it was assumed that the aqueous phase relative permeability for pressure-driven drainage by gas is the same as for drainage driven by gas exsolution. All parameter values are summarized in Table 4 with the relative permeability functions plotted in Fig. 3.

4. Results and discussion

In the simulations reported here, only S_g^{nuc} (see Eq. (6)) and the gas relative permeability parameters S_{gr} and n_g (see Eq. (12)) were considered adjustable. Every other parameter was independently measured or estimated. In what follows, we discuss separately those experimental observations and numerical results which pertain to the time period $t_0 \leq t \leq t_{SWI}$ (SWI transient and steady state) from those pertaining to the time period $t_{SWI} < t \leq t_{\mu-SWI}$ (post-SWI transient), all with reference to experiment #8 (see Tables 1 and 3) against which the continuum model is calibrated. Subsequently, we examine the extent to which the remaining experiments can be predicted using the same set of parameter values ($S_g^{\text{nuc}}, S_{gr}, n_g$). The post-SWI information affords an additional test on the ability of the continuum model to describe gas

exsolution and flow when SWI is stopped, but a driving force for mass transfer remains. This driving force is a consequence of two factors, namely volumetric expansion of the gas phase as pressures return to hydrostatic and an increase in the level of CO₂ supersaturation of the aqueous phase due to the decline in aqueous phase pressure.

4.1. SWI transient and steady state

As shown in Fig. 4, injection of up to ca. 0.5 pore volumes (PV) of CO₂-supersaturated aqueous phase at constant rate is associated with transient behavior of the aqueous phase effluent rate. The latter is seen to increase very rapidly to values greater than Q_q^{inj} , whilst no gas phase is produced. A rapid increase of the injection pressure is also observed as the relative permeability of the aqueous phase is reduced in the presence of gas within the pore space. As soon as SWI is initiated, miscible displacement of the CO₂-free resident aqueous phase by the CO₂-rich injected aqueous phase takes place, resulting in nucleation and growth of the gas phase in the lowest part of the column. As gas saturation develops, a volumetric displacement occurs which is observed as an increase in the aqueous phase effluent rate. The aqueous phase injection rate, Q_q^{inj} , is constant throughout the experiment, which allows for the aqueous phase effluent rate, Q_q^{eff} , to be used as the primary method to calculate the average gas saturation in the column. The total volume of displaced aqueous phase and thus the column-averaged change in gas saturation $\Delta\bar{S}_g$ at time t_{SWI} can be determined as follows:

$$\Delta\bar{S}_g(t_{SWI}) = \int_{t_0}^{t_{SWI}} [Q_q^{eff}(t) - Q_q^{inj}] dt \quad (15)$$

At the end of the transient period, $Q_q^{eff} = Q_q^{inj}$, and the rate of gas accumulation in the column is zero. It is important to note that gas flow out of the column does not begin until the gas saturation is nearly fully developed. The aqueous phase effluent rate, Q_q^{eff} , remains constant thereafter until SWI is terminated at time t_{SWI} , that is after injection of about 6 PV of CO₂-supersaturated aqueous phase. On the contrary, the measured gas flow rate which reaches a maximum once a steady gas saturation is established, is observed to decrease gradually with time as a result of a decreasing mole fraction of dissolved CO₂ in the injected aqueous phase, $X_{CO_2,q}^{inj}$. This

is a consequence of unpredictable variability in the performance of the membrane contactor.

No attempt was made to incorporate temporal changes of $X_{CO_2,q}^{inj}$ in the simulation. Instead, it was assumed that $X_{CO_2,q}^{inj}$ is constant and equal to the value determined experimentally as explained in Section 2. The actual aqueous phase sample used to perform this calculation is shown by the large open circle in Fig. 4. As shown in Fig. 4, the simulation accurately reproduces experimental measurements of aqueous phase effluent flow, gas phase effluent flow, and injection pressure throughout the time period $t_0 \leq t \leq t_{SWI}$. Such agreement was achieved using the gas phase relative permeability function plotted in Fig. 3 and $S_g^{nuc} = 0.03$ in the mass transfer rate expression, Eq. (6). It was found that unless such an *ad hoc* modification of the mass transfer rate expression is made, the continuum model is unable to accurately describe the dynamics of gas accumulation in the column for any choice of gas phase relative permeability. This is to be expected because the kinetics of the initial stages of gas phase formation (nucleation) [18,22], which are not explicitly accounted for in the continuum model, are markedly different from the kinetics of non-equilibrium mass transfer between a flowing aqueous phase and non-wetting gas phase ganglia [23]. Pore network simulations reported in the companion paper [34] also demonstrate sensitivity of the rate of gas saturation growth to the nucleation characteristics of porous media during the initial transient period of SWI, when supersaturation increases.

A more in-depth examination of the experimental observations is possible with the help of the numerical model. Fig. 5 shows again measured and simulated aqueous phase effluent during the initial transient period of SWI. A number of time points of interest to this transient behavior are identified with letters (A, I, and J) in this figure. These points in time are discussed with reference to Fig. 6, which plots the simulated spatiotemporal evolution of gas phase saturation and CO₂ content of the resident aqueous phase. Fig. 6 also presents the mole fraction of dissolved CO₂ at conditions of equilibrium between the gas and aqueous phases, determined from Henry's law (see Eq. (10)) at the prevailing steady-state aqueous phase pressure distribution and temperature T^{eff} . The difference between the bulk and equilibrium CO₂ concentration in the aqueous phase is the driving force for nucleation and subsequent growth of the gas phase. Therefore, Fig. 6 provides insight into: (i) the time evolution of the extent of a macroscopic region in which nucleation and mass transfer-driven *growth* of the gas phase

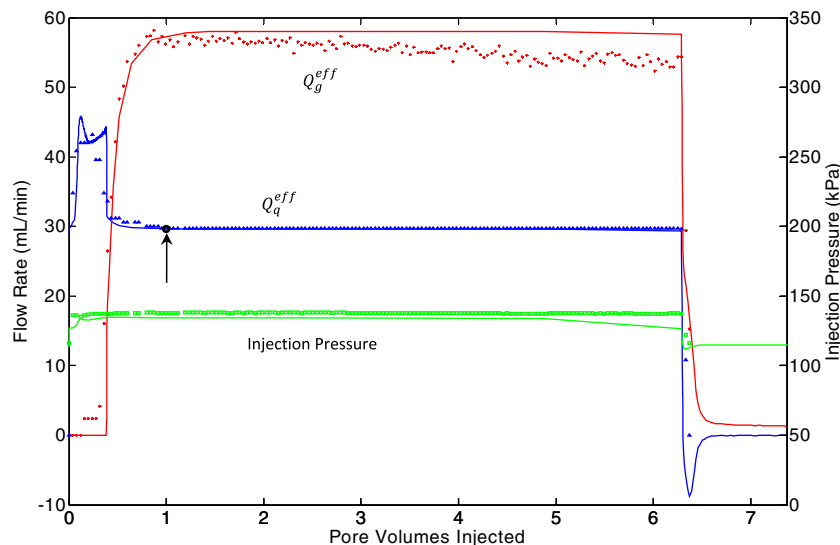


Fig. 4. Experimental (symbols) and simulated (lines) results for experiment #8. The large open circle identified with an arrow at 1 PV of injected aqueous phase denotes the actual aqueous phase effluent sample used to determine $X_{CO_2,q}^{inj}$ as listed on Table 3.

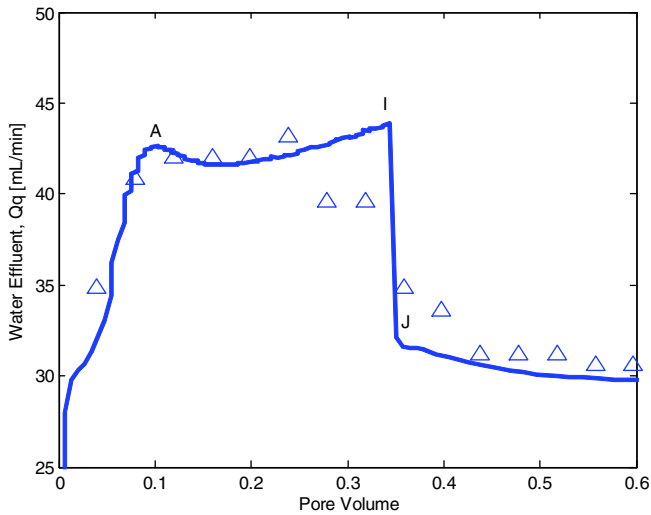


Fig. 5. Experimental (symbols) and simulated (line) aqueous phase effluent rate during SWI as a function of PV of aqueous phase injected (experiment #8): A = 0.10 PV, I = 0.34 PV and J = 0.36 PV.

can take place; and (ii) the development and propagation of a sharp gas saturation front. With the help of Fig. 6, it is straightforward to identify experimental point A in Fig. 5 as the point in time when the gas phase is just inside a zone where nucleation is possible. Thereafter, the gas phase saturation front advances past the zone where CO_2 -supersaturation of the aqueous phase exists. For times past point A during the initial transient stage of SWI, the advancing gas saturation front encounters a resident aqueous phase in which CO_2 from the gas phase can *dissolve* into the aqueous phase, given that the column is initially saturated with a CO_2 -free aqueous phase. This is also surmised from Fig. 7, which plots directly simulation results for \dot{R}_{CO_2} representing the rate of CO_2 exsolution along the column. Here, the rate of exsolution is shown to take on negative values past point A and until steady state is established, implying mass transfer of CO_2 from the gas to the aqueous phase.

Experimental point I in Fig. 5 represents the point in time when a sharp reduction in the rate of gas phase accumulation in the column is observed. As shown in Fig. 6, the simulated gas phase saturation front is very near the top of the column at this time. Point J in Fig. 5 is the point in time when significant gas production is first experimentally observed (see also Fig. 4) and agrees with the simulation results shown in Fig. 6. Furthermore, Fig. 6 shows that the simulated gas phase saturation distribution changes very little after the arrival of the gas saturation front at the top of the column. During this time period, equilibrium partitioning of CO_2 is established at the top part of the column (see Fig. 6) as a result of gas phase dissolution (see Fig. 7). Aqueous phase samples taken at steady state from two sampling ports and analyzed for dissolved CO_2 corroborate the numerical model results (see data points shown as triangles in Fig. 6). At steady state, an average gas saturation of 0.149 is predicted by the continuum model, which is in excellent agreement with the experimental value of $\Delta \bar{S}_g(t_{\text{SWI}}) = 0.145$ as reported on Table 5.

Remarkably, the experimental observations are consistent with a model of compact displacement of the aqueous phase by the exsolved gas. As can be seen in Fig. 6, this displacement is described by advancement of a shock front at $S_g \approx 0.135$, a saturation just higher than the value of the residual gas saturation ($S_{gr} = 0.12$) quantifying the threshold of gas phase mobility. The magnitude of the critical gas saturation, S_{gc} , the saturation associated with the onset of bulk gas flow in pore networks in which gas saturation develops as a result of phase change, has been previously studied by Tsimpanogiannis and Yortsos [31]. In the absence of mass transfer limitations, S_{gc} has been found to be independent of the Bond number, Bo , in the low- Bo range ($Bo < 10^{-4}$) and coincident with the threshold of percolation processes originating from multiple nucleation centers [31]. A consistent estimate of this threshold saturation for our system is fairly tight, $0.12 < S_{gc} < 0.135$. The fact that this estimate is very close to the gas saturation associated with the percolation threshold for drainage of the aqueous phase (see Fig. 2) is not surprising considering the prevailing low Bond number [31]. As regards displacement patterns at the macroscopic scale, gas–liquid two-phase flow during SWI is markedly different from gas–liquid flow during IAS, the latter generally characterized by

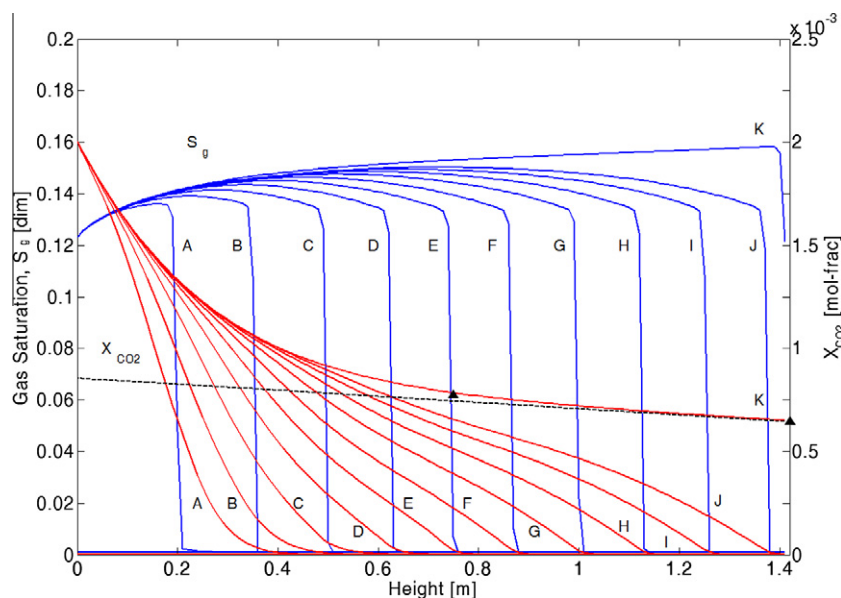


Fig. 6. Simulated gas phase saturation (solid blue lines), S_g , and mole fraction of dissolved CO_2 (solid red lines), $X_{\text{CO}_2,g}$, as functions of column height for experiment #8 at different times: A = 0.10 PV, B = 0.13 PV, C = 0.16 PV, D = 0.19 PV, E = 0.22 PV, F = 0.25 PV, G = 0.28 PV, H = 0.30 PV, I = 0.34 PV, and J = 0.36 PV. The dashed line represents the mole fraction of dissolved CO_2 in equilibrium with the gas phase ($X_{\text{CO}_2,g}$). Symbols (filled triangles) represent measurements of aqueous phase CO_2 mol fraction at time $t = t_{\text{SWI}}$. (For interpretation of the references to color in this figure legend, the reader is referred to the web version of this article.)

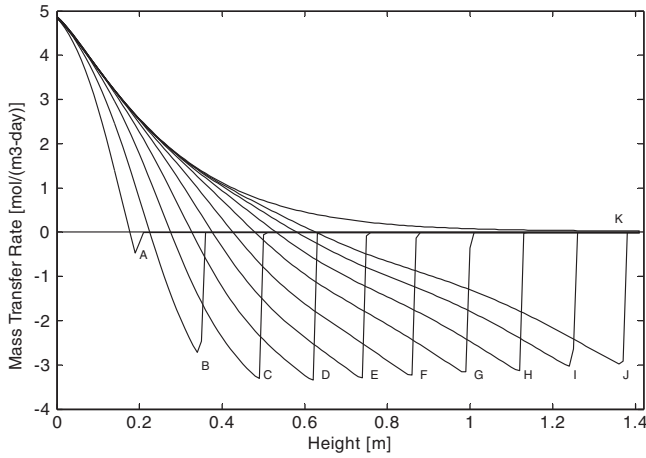


Fig. 7. Simulated mass transfer rate of carbon dioxide from the aqueous to the gas phase (given by \dot{R}_{CO_2} from Eq. (5)) as a function of column height for experiment #8 at different times: A = 0.10 PV, B = 0.13 PV, C = 0.16 PV, D = 0.19 PV, E = 0.22 PV, F = 0.25 PV, G = 0.28 PV, H = 0.30 PV, I = 0.34 PV, J = 0.36 PV, and steady state (K).

Table 5

Column-average gas phase saturation and associated inlet aqueous phase CO_2 -supersaturation changes during and after SWI from experiments and simulations.

Experiment ID	$\Delta \mathcal{S}_f$	Observed $\Delta \bar{S}_g$	Predicted $\Delta \bar{S}_g$	Prediction error $\Delta \bar{S}_g$
$t_0 \leq t \leq t_{\text{SWI}}$	$t = t_0$	$t = t_{\text{SWI}}$	$t = t_{\text{SWI}}$	
1	2.42	0.173	0.163	0.010
2	2.16	0.130	0.158	-0.028
3	2.47	0.152	0.150	0.002
4	2.46	0.177	0.154	0.023
5	2.19	0.167	0.144	0.023
6	2.44	0.169	0.152	0.017
7	2.43	0.140	0.146	-0.006
8	2.32	0.145	0.149	-0.003
9	2.24	0.148	0.140	0.008
$t_{\text{SWI}} < t \leq t_{\mu\text{-SWI}}$	$t > t_{\text{SWI}}$	$t = t_{\mu\text{-SWI}}$	$t = t_{\mu\text{-SWI}}$	
1	1.42	0.104	0.039	0.065
2	1.28	0.094	0.042	0.052
3	0.27	0.031	0.007	0.024
4	0.32	0.045	0.005	0.040
5	0.19	0.028	0.003	0.025
6	0.35	0.040	0.005	0.035
7	0.21	0.024	0.004	0.020
8	0.33	0.034	0.007	0.027
9	0.15	0.013	0.003	0.010

channeling of the injected gas phase [4,6,9,27,28]. During SWI, the basic premise of a continuum-scale description, namely the existence of a macroscopic representative elementary volume (REV) for gas saturation, is evidently ascertained by the uniform nature of gas phase exsolution.

The continuum model can describe quantitatively all observations associated with experiment #8, subject only to adjustment of parameters affecting the gas relative permeability (S_{gr} and n_g in Eq. (14)) and mass transfer rate at the initial stage of gas phase formation (S_g^{nucl} in Eq. (6)), as mentioned above. The sensitivity of these parameters to changes of particle size, flow rate and dissolved CO_2 concentration of the injected aqueous phase is, of course, of great interest. Considering that gas phase advection during SWI takes place via a repeated sequence of mobilization, fragmentation and coalescence of large gas clusters [34], we hypothesized that the aforementioned parameters would be relatively insensitive to changes of grain size, flow rate and dissolved CO_2 concentration of the injected aqueous phase, as long as the

Bond number characterizing different systems is sufficiently small ($Bo < 10^{-4}$). To test this hypothesis, we simulated two additional experiments (experiments #7 and #9, see Tables 1 and 3) in the same glass bead pack as the one used in experiment #8, and six SWI experiments in uniform sand packs of different permeability (experiments #1–6, see Tables 1 and 3) using the same parameters (see Table 4).

A visual assessment of the ability of the continuum model to predict SWI experiments in packed columns is shown in Fig. 8 with reference to experiment #6. Similar results were obtained for all other experiments and are not shown. In each case, the continuum model provides a reasonable prediction of the gas and water effluent rates and injection pressure. A quantitative assessment of the predictive ability of the continuum model is given in Table 5 in terms of the column-average change in gas phase saturation, $\Delta \bar{S}_g$, established in the columns during SWI at steady state as determined by Eq. (15). On average, the simulation underestimates the experimentally observed change of gas saturation at steady state in sand-packed columns by less than 0.02, whereas it is within 0.01 for the column filled with glass beads. In all experiments considered, gas exsolution occurs only in the bottom half of the column. In addition, the aqueous phase effluent is at equilibrium with a pure CO_2 gas phase at P^{ref} which is the pressure at the column outlet. On the basis of these findings, the hypothesis that gas relative permeability during SWI is relatively insensitive to the grain size, injected aqueous phase flow rate and dissolved CO_2 concentration cannot be rejected. Notwithstanding, we remind the reader that these parameters were varied within narrow ranges and further testing is necessary.

4.2. Post-SWI transient

With no exception, the gas effluent rate is observed to decay very rapidly to zero as soon as injection of the CO_2 -supersaturated aqueous phase is stopped (see Figs. 4 and 8). The same is true of the aqueous phase effluent rate and relevant experimental data are detailed in Fig. 9. Careful consideration of these observations affords us additional insight into the strengths and limitations of the proposed continuum-level description of gas exsolution and flow during SWI.

The experimental data plotted in Fig. 9 indicate that there is further change (increase) of column-average gas saturation, which is given by the following equation:

$$\Delta \bar{S}_g(t_{\mu\text{-SWI}}) = \int_{t_{\text{SWI}}}^{t_{\mu\text{-SWI}}} Q_q^{\text{eff}}(t) dt \quad (16)$$

where $t_{\text{SWI}} < t \leq t_{\mu\text{-SWI}}$ is the post-SWI observation time period and $\Delta \bar{S}_g(t_{\mu\text{-SWI}})$ represents the change in the column averaged gas saturation during this time. Once SWI is terminated, the pressure of the column is suddenly reduced to hydrostatic (see Table 3). A first consequence of a reduction in liquid pressure is volumetric expansion of the gas phase and therefore displacement of some of the aqueous phase. This consequence is accounted for in the continuum model. Other consequences are related to additional gas phase formation (nucleation) and mass transfer-driven growth as explained below.

Both nucleation and mass transfer are processes linked to departure from thermodynamic equilibrium as measured, for example, by the following ratio of CO_2 mole fractions in the aqueous phase:

$$\mathcal{S}_f = \frac{X_{\text{CO}_2q}}{X_{\text{CO}_2q}^*} \quad (17)$$

where X_{CO_2q} and $X_{\text{CO}_2q}^*$ represent the actual and equilibrium CO_2 content of the aqueous phase and $\mathcal{S}_f > 1$ denotes supersaturation. The degree of supersaturation varies with location and is highest at

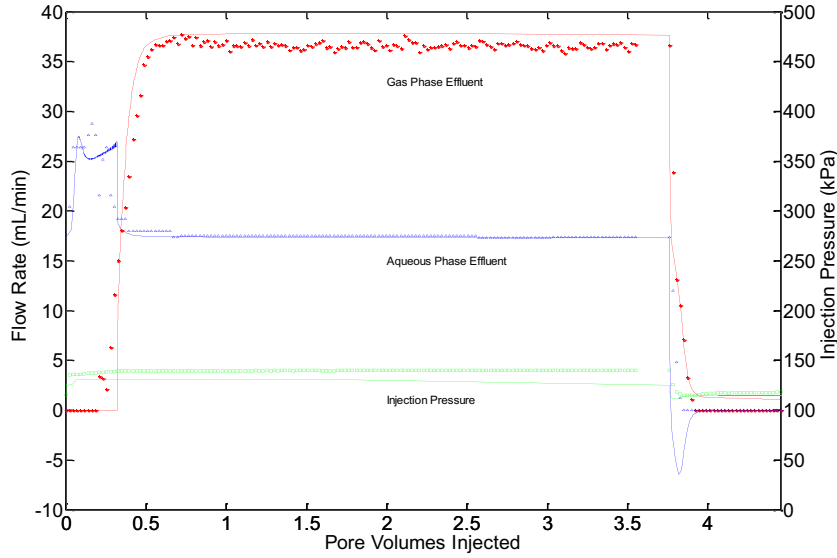


Fig. 8. Experimental (symbols) and simulated (lines) results for experiment #6.

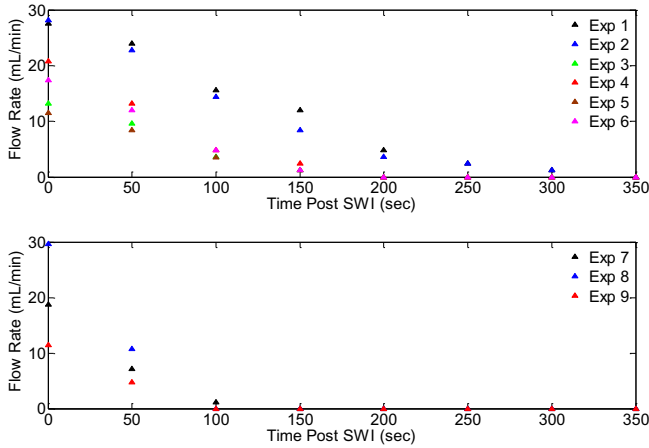


Fig. 9. Observed aqueous phase effluent rates for the post-SWI transient, $Q_q^{eff}(t)$ in Eq. (16), for sand and glass bead column experiments.

the base of the column, where it may be readily estimated from knowledge of the aqueous phase pressure. Assuming that the reduction of the column pressure to hydrostatic (i.e., $P_g(t_{SWI}) \rightarrow P_g(t_{\mu-SWI})$) is instantaneous, the mole fraction of CO_2 in the aqueous phase at the bottom of the column remains unchanged and is equal to $X_{\text{CO}_2q}^{inj}$. We can therefore estimate the change $\Delta\mathcal{S}_f$ in the degree of supersaturation realized by the sudden reduction in the pressure of the aqueous phase as follows:

$$\Delta\mathcal{S}_f = \frac{X_{\text{CO}_2q}^{inj}}{X_{\text{CO}_2q}^*|P_g(t_{\mu-SWI})} - \frac{X_{\text{CO}_2q}^{inj}}{X_{\text{CO}_2q}^*|P_g(t_{SWI})} \quad (18)$$

As shown in Table 5, reduction of the aqueous phase pressure to hydrostatic causes an increase in the degree of supersaturation at the base of the column. In turn, this implies an increase in the driving force for CO_2 transfer from the aqueous to the gas phase (see Eq. (5)), resulting from a decrease in P_g in Eq. (10), which is accounted for in the continuum model. Another, rather distinct, implication is gas phase formation at a number of nucleation sites not previously activated leading to the appearance of gas phase in pores which at the conclusion of SWI contained only aqueous phase. This implication is consistent with progressive nucleation theory [22], according

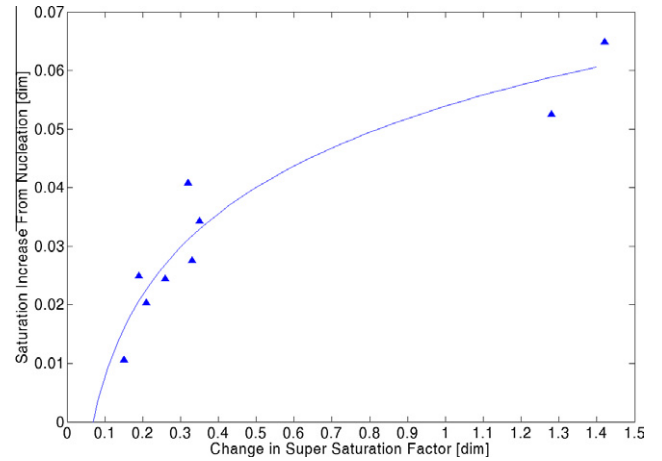


Fig. 10. Observed increase in gas phase saturation after SWI that is not accounted for in the simulation and is attributed to nucleation. This is quantified as the difference between observed and simulated increase in gas phase saturation $\Delta\bar{S}_g(t_{\mu-SWI})$ and plotted against the change in the supersaturation factor $\Delta\mathcal{S}_f$ as defined by Eq. (18) and listed in Table 5. Solid line is only a guide to the eye.

to which each nucleation site is activated at a different supersaturation threshold. Our *ad hoc* fix to the Nambi and Powers model, S_g^{nuc} , which was found adequate for describing the rapid increase in gas saturation due to nucleation at the initial stage of SWI, has no effect at the post-SWI stage given that the gas phase saturation in the column is above 0.03 (see Table 4). Table 5 shows that, in every case, the simulation *underestimates* the post-SWI gas saturation growth $\Delta\bar{S}_g$ by an amount that is an increasing function of $\Delta\mathcal{S}_f$, as shown in Fig. 10. This finding is consistent with progressive nucleation theory [22]. It also illustrates a limitation in the way the effects of nucleation are presently handled in the continuum model, which we plan to address in a forthcoming communication following related work by Tsimpanogiannis and Yortsos [30].

5. Conclusions

We carried out a first investigation of the process of CO_2 -supersaturated water injection (SWI) in water-saturated porous media by means of experiments in homogeneous columns packed with

glass beads or silica sand and continuum-scale simulation. This study addressed aspects of two-phase flow and mass transfer at the macroscopic scale, strengthening and extending a number of conclusions reached in the first part of this work [34], where CO₂-supersaturated water injection was studied by pore network simulation. A multiphase compositional model (CompFlow-SWI) was employed to interpret the experimental observations, leading to the following conclusions:

- Initial formation (nucleation) and growth of the CO₂ gas phase during SWI is associated with the development of an exsolution zone of finite extent near the point of injection. Rate-limited transfer of CO₂ from the aqueous to the gas phase is adequately described at the macroscopic scale by a published correlation due to Nambi and Powers [23], but an *ad hoc* modification of this correlation to account for heterogeneous nucleation is only partially successful.
- Gas phase accumulating within the exsolution zone becomes mobile at a critical value of gas saturation which, for the media studied in this work, is close to the breakthrough gas saturation for drainage of the aqueous phase (*ca.* 0.14). Advection of the gas phase is consistent with the advancement of a sharp front and can be predicted by the classical extension of Darcy's law to two-phase flow. The associated gas phase relative permeability is determined and found to be insensitive to changes in particle size and injection flow rate.

The finding that displacement of the aqueous phase by gas is compact at the macroscopic scale is consistent with a pore-level description of the SWI process, according to which gas phase propagation under conditions of small Bond number results from repeated mobilization, fragmentation and coalescence of large gas clusters (i.e., large ganglion dynamics) driven entirely by mass transfer. The apparent success of a Darcy-based model of gas phase mobility hinges on the existence of a representative elementary volume (REV) for gas saturation, which is assured by the uniform nature of nucleation and mass transfer-driven growth of a gas phase in porous media. This is likely a significant advantage of SWI over gas sparging, which generally results in channelized gas flow.

Acknowledgements

Financial support for this work by the Ontario Centers of Excellence (OCE) and the Natural Sciences and Engineering Research Council of Canada (NSERC), as well as in-kind support by InVentes Technologies Inc., is gratefully acknowledged.

References

- [1] Avraam DG, Payatakes AC. Flow regimes and relative permeabilities during steady-state 2-phase flow in porous media. *J Fluid Mech* 1995;293:207–36.
- [2] Avraam DG, Payatakes AC. Generalized relative permeability coefficients during steady-state 2-phase flow in porous media and correlation with the flow mechanisms. *Transport Porous Med* 1995;20:135–68.
- [3] Bass DH, Hastings NA, Brown RA. Performance of air sparging systems: a review of case studies. *J Hazard Mater* 2000;72:101–19.
- [4] Brooks MC, Wise WR, Annable MD. Fundamental changes in in-situ air sparging flow patterns. *Ground Water Monit Rem* 1999;19(2):105–13.
- [5] Buckley SE, Leverett MC. Mechanism of fluid displacements in sands. *Trans AIME* 1942;146:107–16.
- [6] Chen M-R, Hinkley RE, Killough JE. Computed tomography imaging of air sparging in porous media. *Water Resour Res* 1996;32(10):3013–24.
- [7] Corey AT. The interrelation between gas and oil relative permeabilities. *Prod Mon* 1954;19(1):38–41.
- [8] D'Azvedo EF, Forsyth PA, Tang W-P. Towards a cost-effective high order ILU preconditioner. *BIT* 1992;32:442–63.
- [9] Elder CR, Benson CH. Air channel formation, size, spacing and tortuosity during air sparging. *Ground Water Monit Rem* 1999;19(3):171–81.
- [10] Forsyth PA. A positivity-preserving method for simulation of steam injection for NAPL site remediation. *Adv Water Resour* 1993;16:351–70.
- [11] Forsyth PA, Shao BY. Numerical simulation of gas venting for NAPL site remediation. *Adv Water Resour* 1991;14:354–67.
- [12] Forsyth PA, Unger AJA, Sudicky EA. Nonlinear iteration methods for nonequilibrium multiphase subsurface flow. *Adv Water Resour* 1998;21:433–49.
- [13] Fry VA, Selker JS, Gorelick SM. Experimental investigations for trapping oxygen gas in saturated porous media for in situ bioremediation. *Water Resour Res* 1997;33(12):2687–96.
- [14] Geistlinger H, Lazik D, Krauss G, Vogel H-J. Pore-scale and continuum modeling of gas flow pattern obtained by high-resolution optical bench-scale experiments. *Water Resour Res* 2009;45. doi:10.1029/2007WR006548.
- [15] Ioannidis MA, Chatzis I, Lemaire C, Perunarkilli R. Unsaturated hydraulic conductivity from nuclear magnetic resonance measurements. *Water Resour Res* 2006;42:W07201. doi:10.1029/2006WR004955.
- [16] Ji W, Dahmani A, Ahfeld DP, Lin JD, Hill E. Laboratory study of air sparging: air flow visualization. *Ground Water Monit Rem* 1993;13(4):115–26.
- [17] Johnson RL, Johnson PC, McWhorter DB, Hinchey RE, Goodman I. An overview of in situ air sparging. *Ground Water Monit Rem* 1993;13(4):127–35.
- [18] Kashchiev D, Firoozabadi A. Kinetics of the initial stage of isothermal gas phase formation. *J Chem Phys* 1993;98(6):4690–9.
- [19] Klotz D, Seiler K-P, Moser H, Neumaier F. Dispersion and velocity relationship from laboratory and field experiments. *J Hydrol* 1980;45:169–84.
- [20] Leverett MC. Capillary behaviour in porous solids. *Trans AIME* 1941;142:159–72.
- [21] Li TMW, Ioannidis MA, Chatzis I. Recovery of non-aqueous phase liquids from ground sources. United States patent #7300227; 2007.
- [22] Li X, Yortsos YC. Visualization and simulation of bubble growth in pore networks. *AIChE J* 1995;41(2):214–22.
- [23] Nambi IM, Powers SE. Mass transfer correlations for nonaqueous phase liquid dissolution from regions with high initial saturations. *Water Resour Res* 2003;39(2):1030. doi:10.1029/2001WR000667.
- [24] Nelson LC, Barker J, Li T, Thomson N, Ioannidis M, Chatzis I. A field trial to assess the performance of CO₂-supersaturated water injection for residual volatile LNAPL recovery. *J Contam Hydrol* 2009;109:82–90.
- [25] Saad Y, Schultz M. GMRES: a generalized minimum residual algorithm for solving nonsymmetric linear systems. *SIAM J Sci Statist Comput* 1986;7:856–69.
- [26] Selker JS, Niemet M, McDuffie NG, Gorelick SM, Parlange JY. The local geometry of gas injection into saturated homogeneous porous media. *Transport Porous Med* 2007;68(1):107–27.
- [27] Stauffer F, Kong XZ, Kinzelbach W. A stochastic model for air injection in porous media. *Adv Water Resour* 2009;32(8):1180–6.
- [28] Stohr M, Khalili A. Dynamic regimes of buoyancy-affected two-phase flow in unconsolidated porous media. *Phys Rev E* 2006;73:036301.
- [29] Thomson NR, Johnson RL. Air distribution during in situ air sparging: an overview of mathematical modeling. *J Hazard Mater* 2000;72:265–82.
- [30] Tsimpanogiannis IN, Yortsos YC. Model for the gas evolution in a porous medium driven by solute diffusion. *AIChE J* 2002;48(11):2690–710.
- [31] Tsimpanogiannis IN, Yortsos YC. The critical gas saturation in a porous medium in the presence of gravity. *J Colloid Interface Sci* 2004;270(2):388–95.
- [32] Unger AJA, Forsyth PA, Sudicky EA. Influence of alternative dissolution models and subsurface heterogeneity on DNAPL disappearance times. *J Contam Hydrol* 1998;30:217–42.
- [33] van der Vorst HA. Bi-CGSTAB: a fast a smoothly converging variant of BiCG for the solution of nonsymmetric linear systems. *SIAM J Sci Statist Comput* 1992;13:631–45.
- [34] Zhao W, Ioannidis MA. Gas exsolution and flow during supersaturated water injection in porous media: I. Pore network modeling. *Adv Water Resour* 2011;34(1):2–14.



CO₂ Supersaturated Water Injection for Enhanced NAPL Recovery in Source Zones

Acknowledgements

- Marios A. Ioannidis, PhD
Director, Nanotechnology
University of Waterloo, Ontario, CA
mioannid@uwaterloo.ca
- John H. Archibald, P.Eng.
inVentures Technologies inc.
john.archibald@inventures.ca



CO₂ SWI Demo

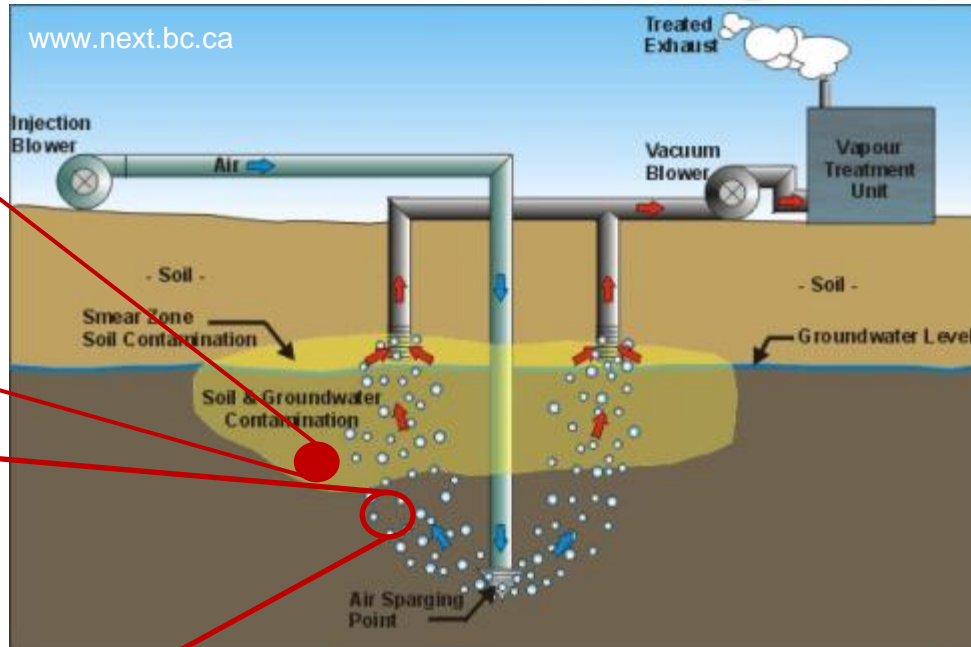
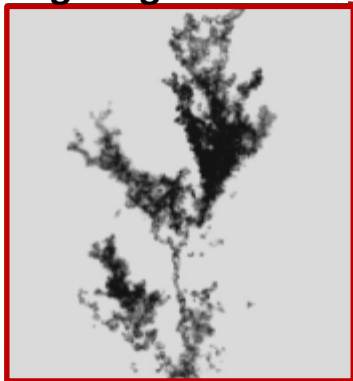


NAPL Source Zone Challenges

Trapped free-phase LNAPL



Air channeling / fingering



➤ Poor access of injected air to residual NAPL

Slide courtesy of Marios A. Ioannidis

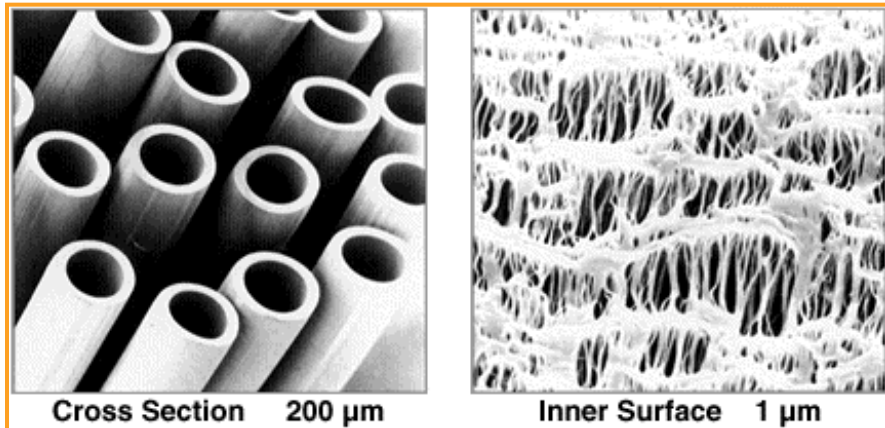
tersusenv.com

Copyright © 2012 Tersus Environmental, LLC. All Rights Reserved.



Gas inFusion™ iSOC® Technology

Microporous Hollow Fiber



- Mass transfer device
- Supersaturates treatment well without sparging
- Bioremediation stimulated by delivery of substrates

iSOC®



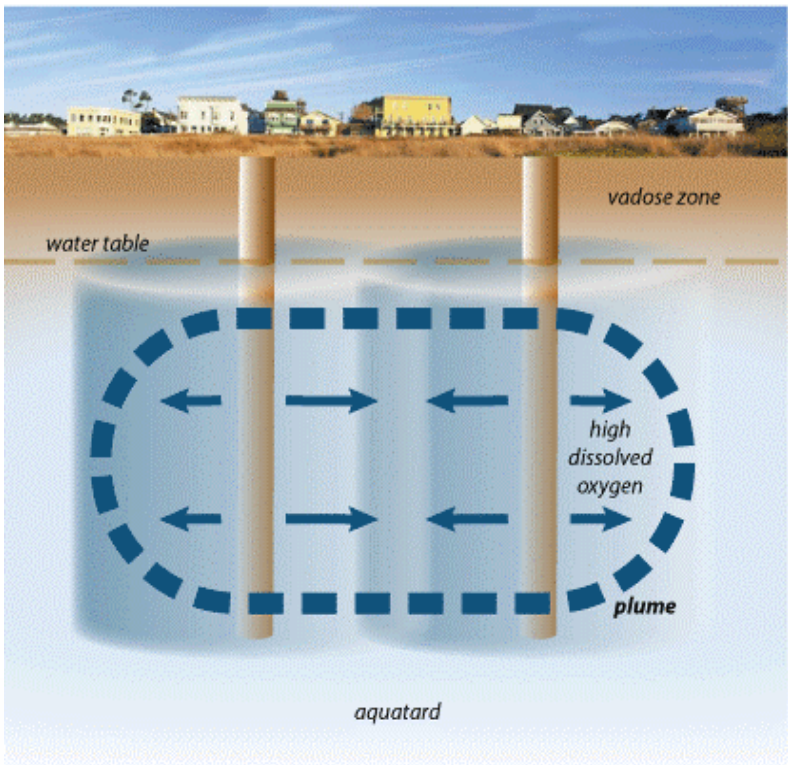
tersusenv.com

Copyright © 2011 Tersus Environmental, LLC. All Rights Reserved.

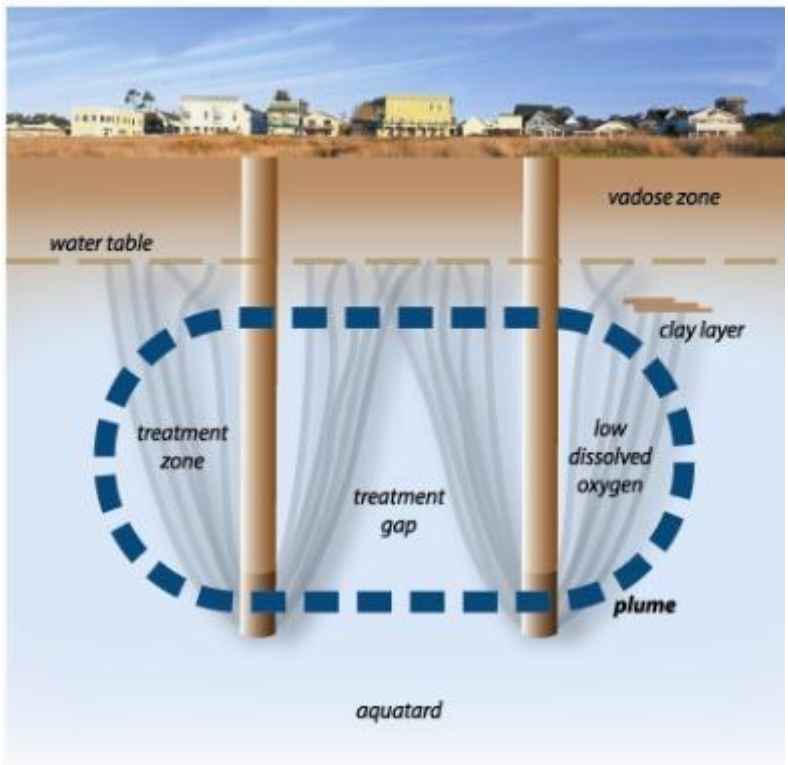


iSOC® Area of Influence

iSOC® Gas Infusion



Air Sparging

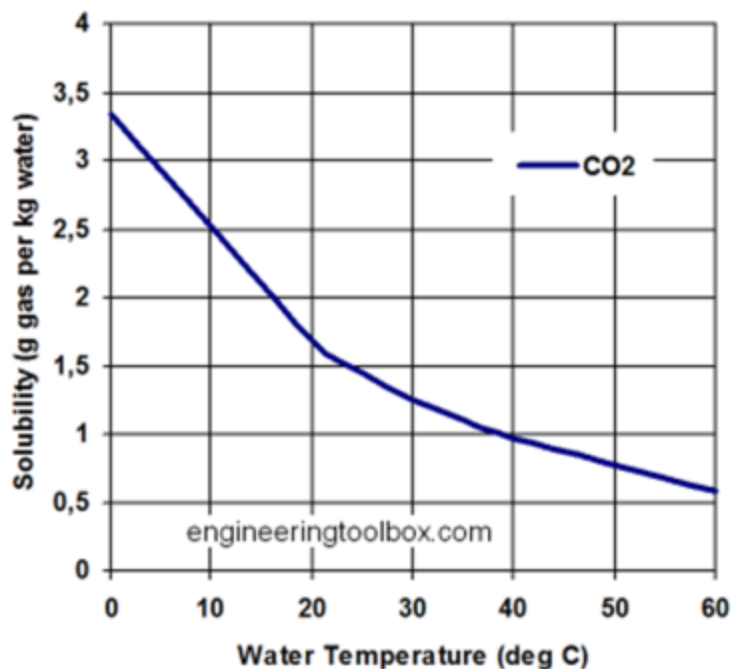


Dissolved Gas Concentrations

Gas Type	Water Column Depth in Feet (Dissolved Gas in ppm)				
	5'	10'	15'	20'	50'
Oxygen	42	55	62	69	111
Methane	22	30	33	37	59
Propane	66	88	99	110	175
Hydrogen	2	2	3	3	5
Ethane	57	75	85	95	150
Carbon Dioxide	1,660	1,875	2,090	2,300	3,590



Solubility of CO₂ in Water



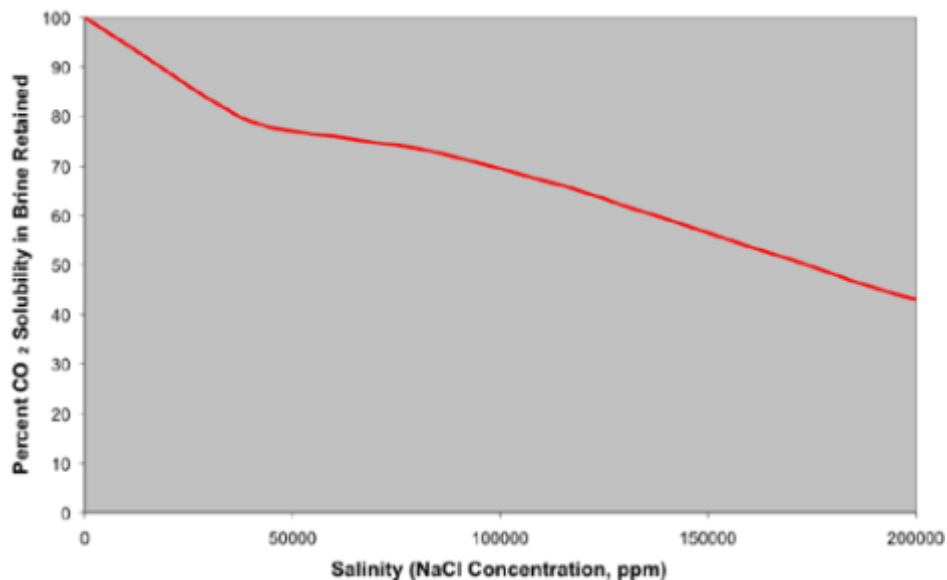
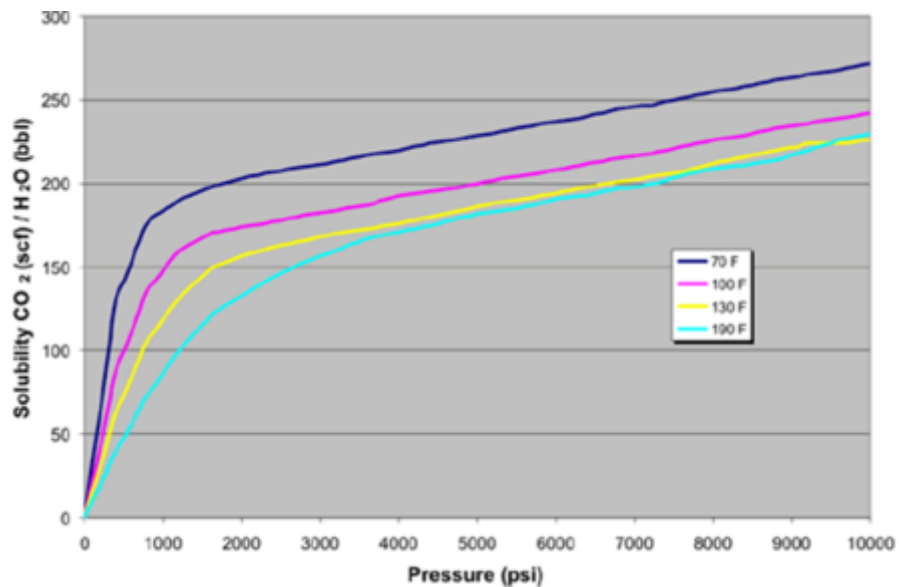
- 2,300 ppm at 12°C (54°F), 1 atmosphere
- 1,450 ppm at 25°C (72°F), 1 atmosphere



Ref: engineeringtoolbox.com
tersusenv.com

Copyright © 2011 Tersus Environmental, LLC. All Rights Reserved.

Solubility of CO₂ in Water



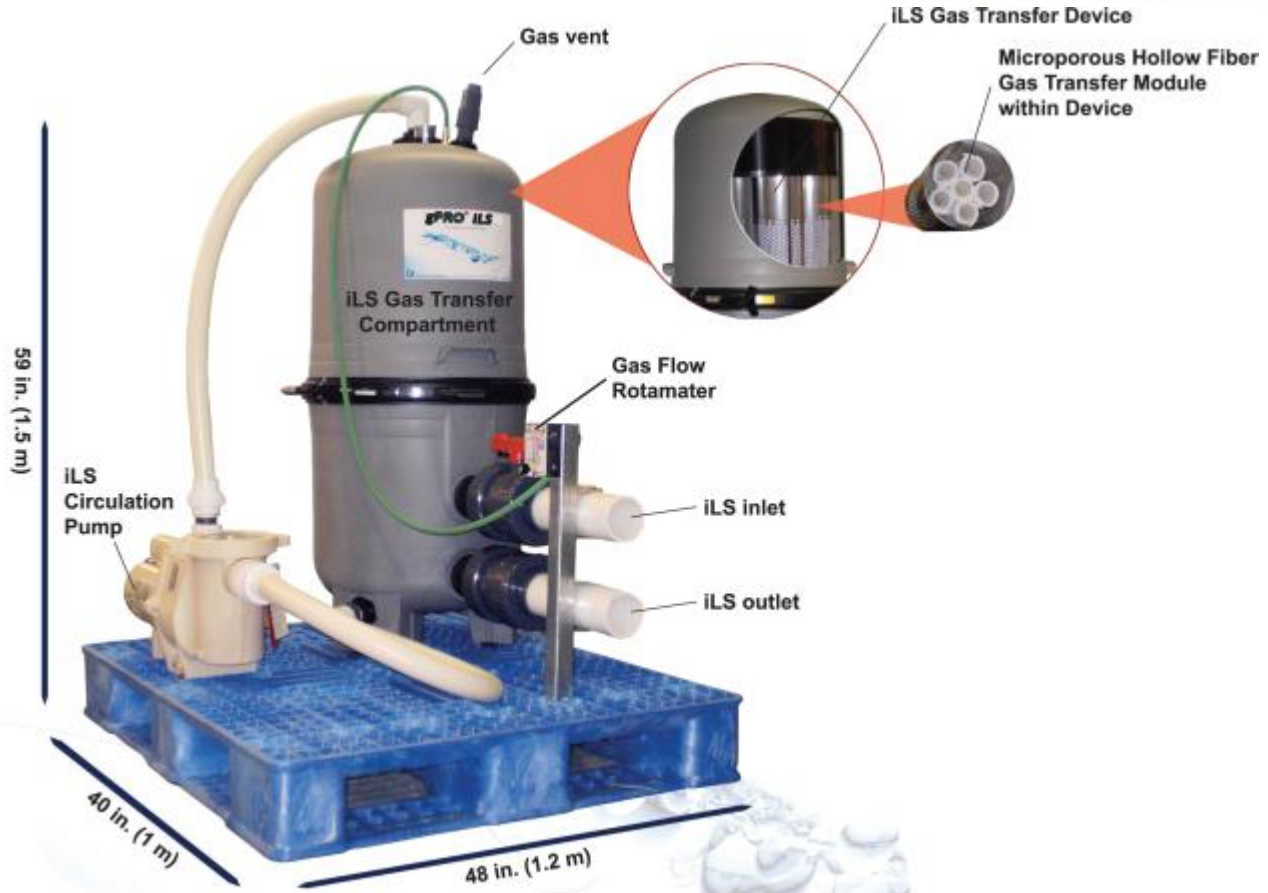
Ref: Kansas Geological Survey

tersusenv.com

Copyright © 2012 Tersus Environmental, LLC. All Rights Reserved.

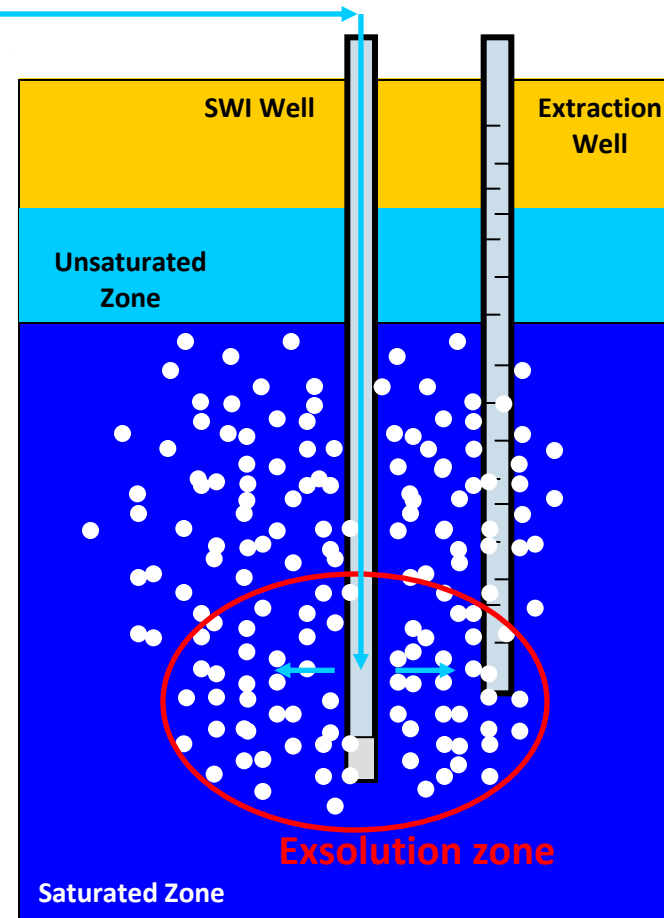


gPRO iLS Gas Transfer System



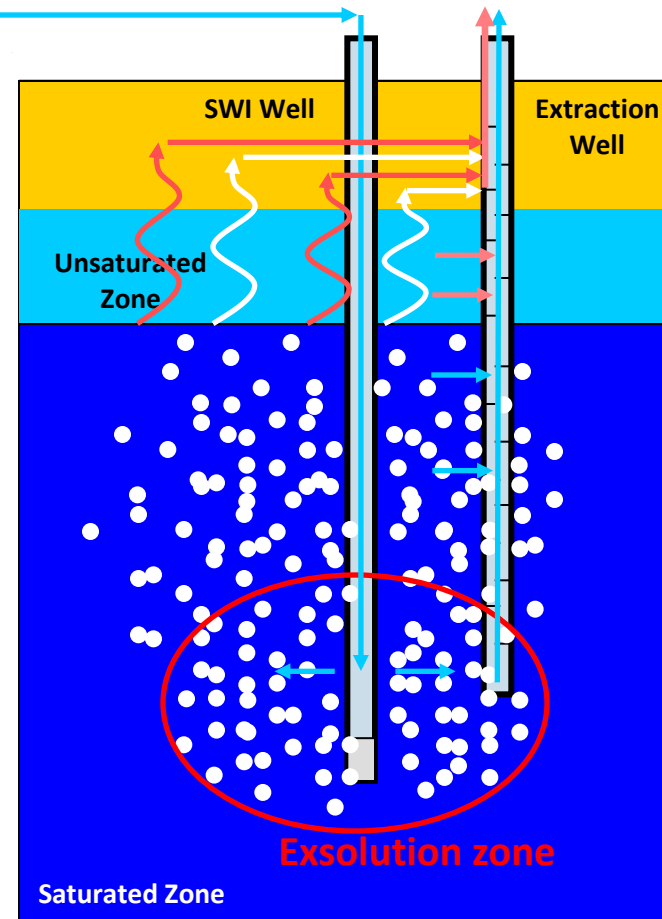
Supersaturated Water Injection

- Water is supersaturated with CO₂
- Supersaturated water is then injected into the aquifer
- CO₂ bubbles nucleate in the aquifer



Conceptual Model

- Rising CO₂ bubbles
 - Contact hydrocarbons
 - Cause volatilization
- Groundwater and soil vapor are extracted



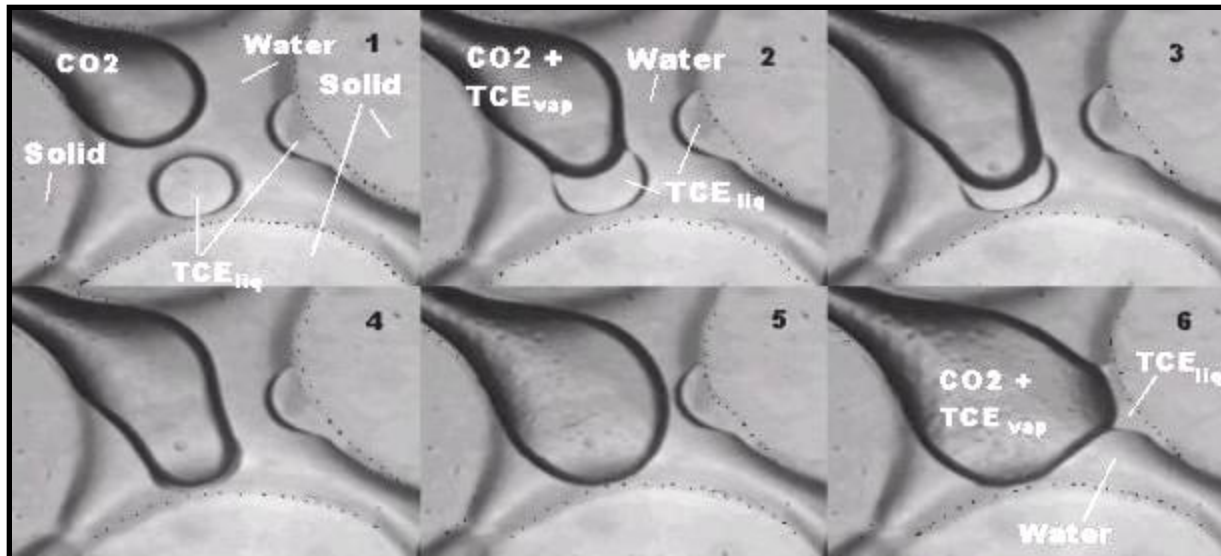
- Zhao and Ioannidis, *Advances in Water Resources*, vol. 34 (1), 2- 14, 2011
- Enouy et al., *Advances in Water Resources*, vol. 34 (1), 15-25, 2011

tersusenv.com

Copyright © 2011 Tersus Environmental, LLC. All Rights Reserved.



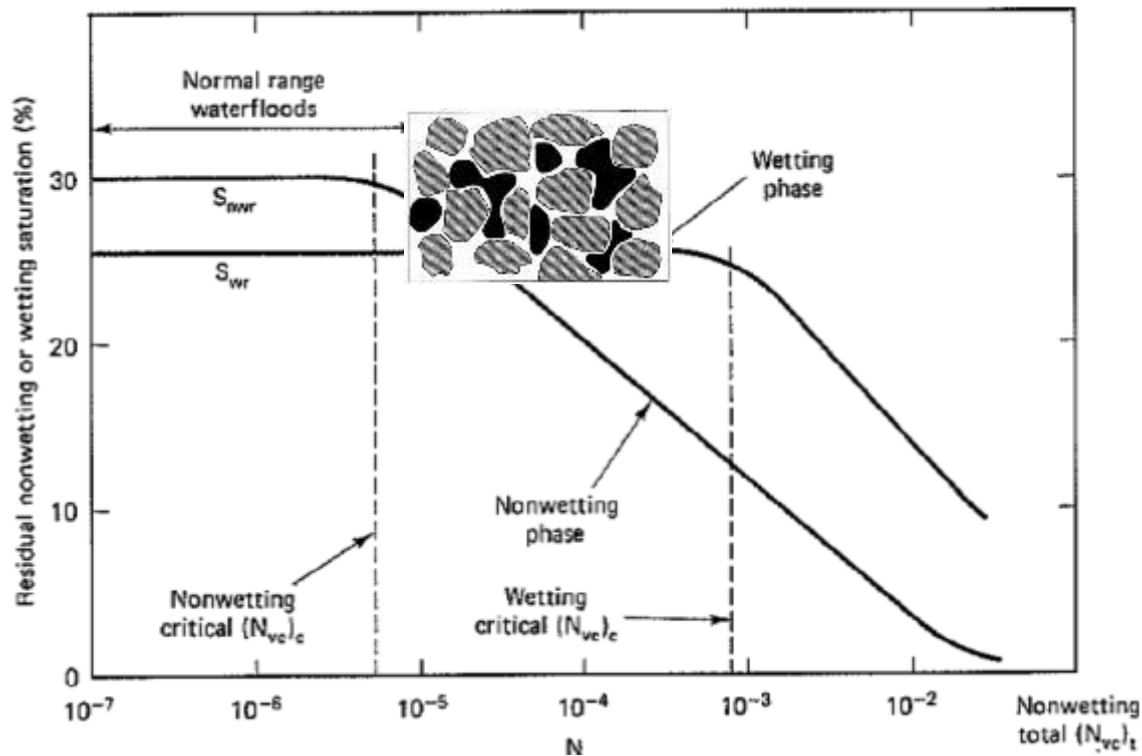
Direct Pore-Scale Evidence of Volatilization



- A CO₂ bubble growing by mass transfer from the injected supersaturated aqueous phase
- Upon contact with the bubble, NAPL spontaneously spreads over bubble
- Volatile components of the NAPL are readily transferred into the bubble



Mobilization of Residual Oil during SWI



A non-wetting phase trapped in the form of ganglia cannot be mobilized during water flooding under normal conditions

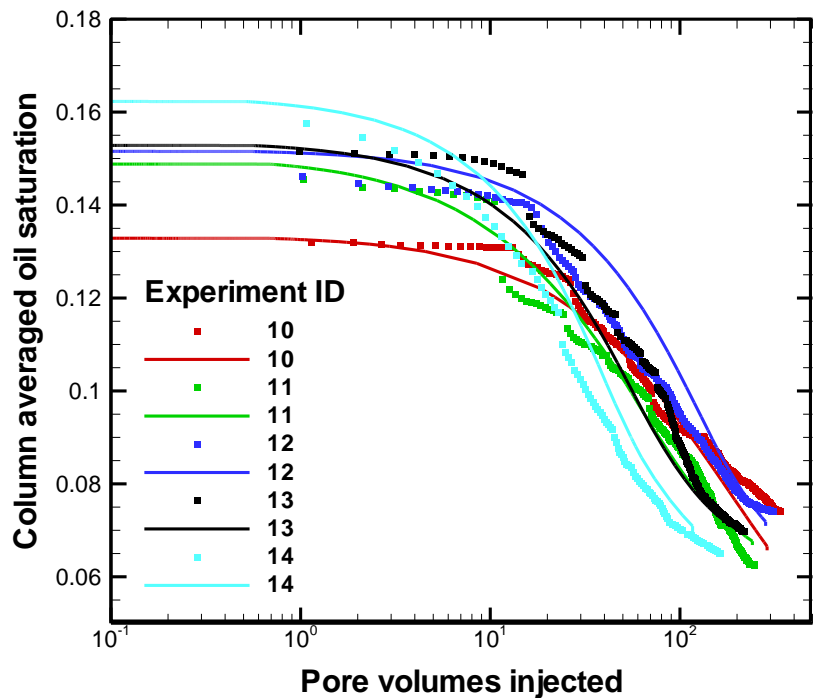
$(N_{ca} = \mu u / \gamma_{ow} < 10^{-5})$, BUT

Slide courtesy of Marios A. Ioannidis

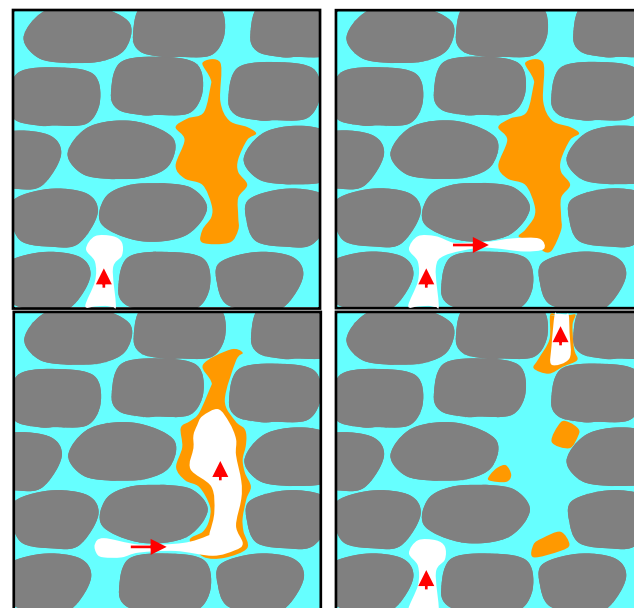
tersusenv.com

Copyright © 2012 Tersus Environmental, LLC. All Rights Reserved.

Mobilization of Residual Oil during SWI



SWI results in **mobilization** and significant **recovery** of residual NAPL (kerosene-hexadecane mixtures) from long sand-packed columns



Mechanism hypothesized

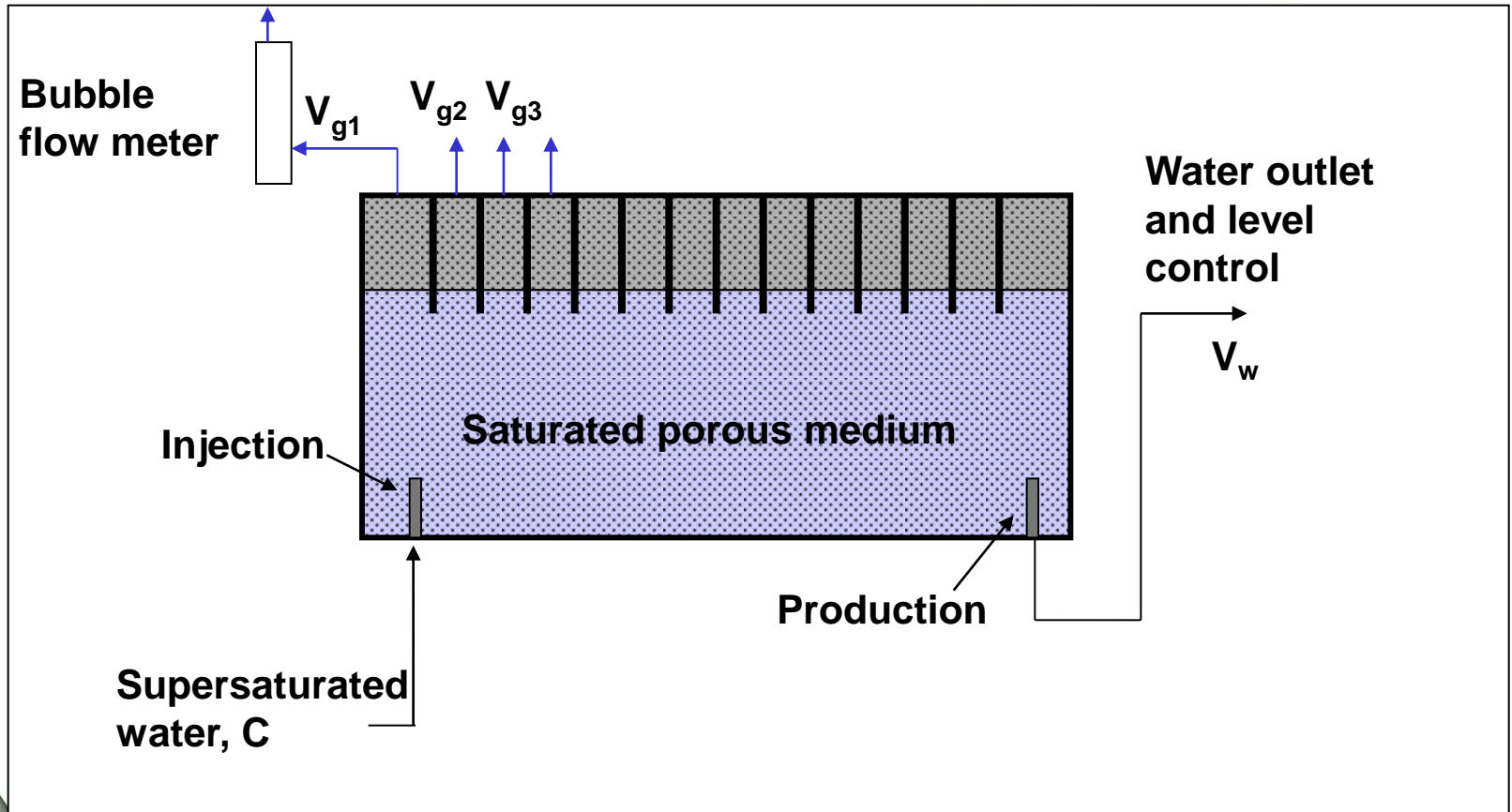
Slide courtesy of Marios A. Ioannidis

tersusenv.com

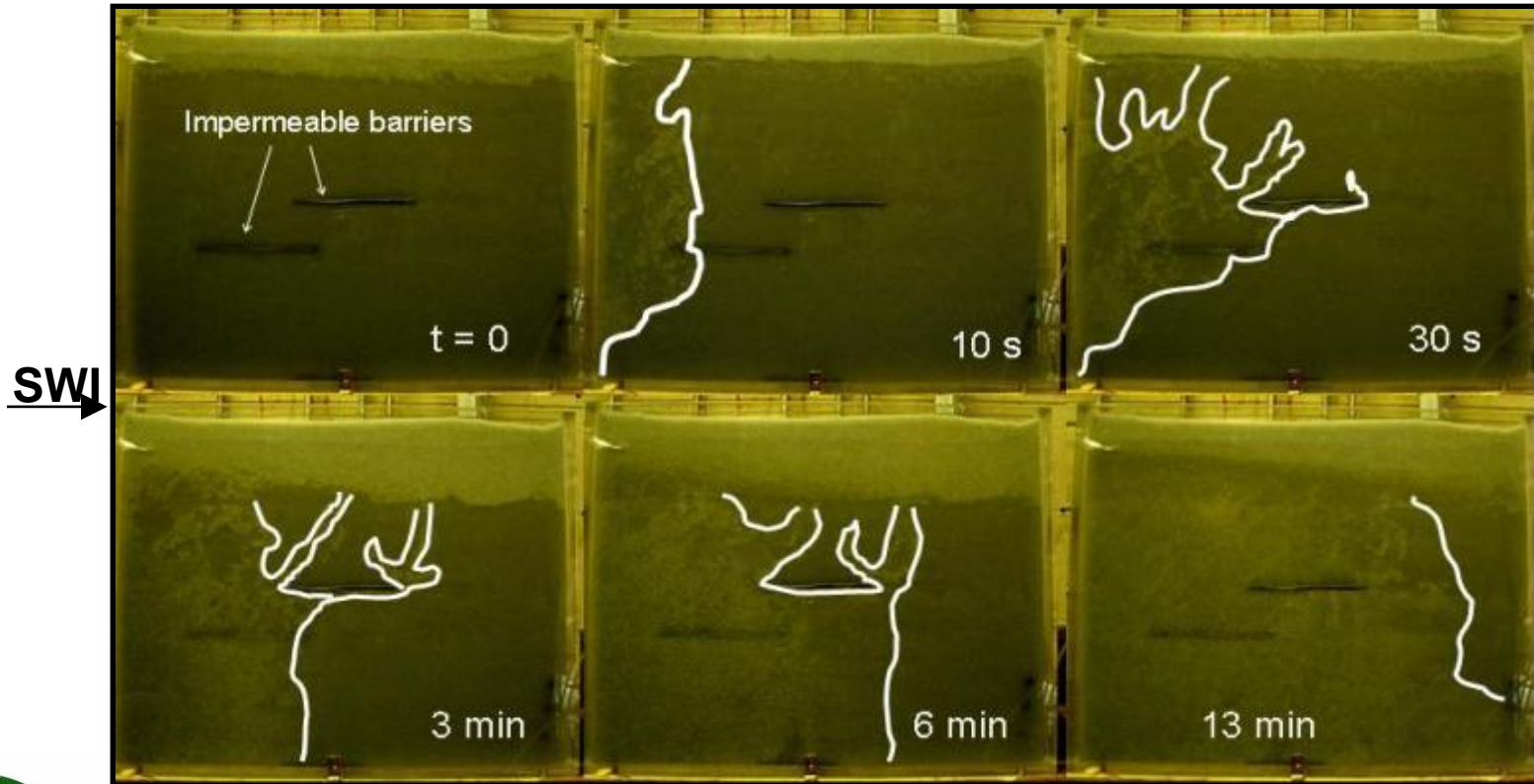
Copyright © 2012 Tersus Environmental, LLC. All Rights Reserved.



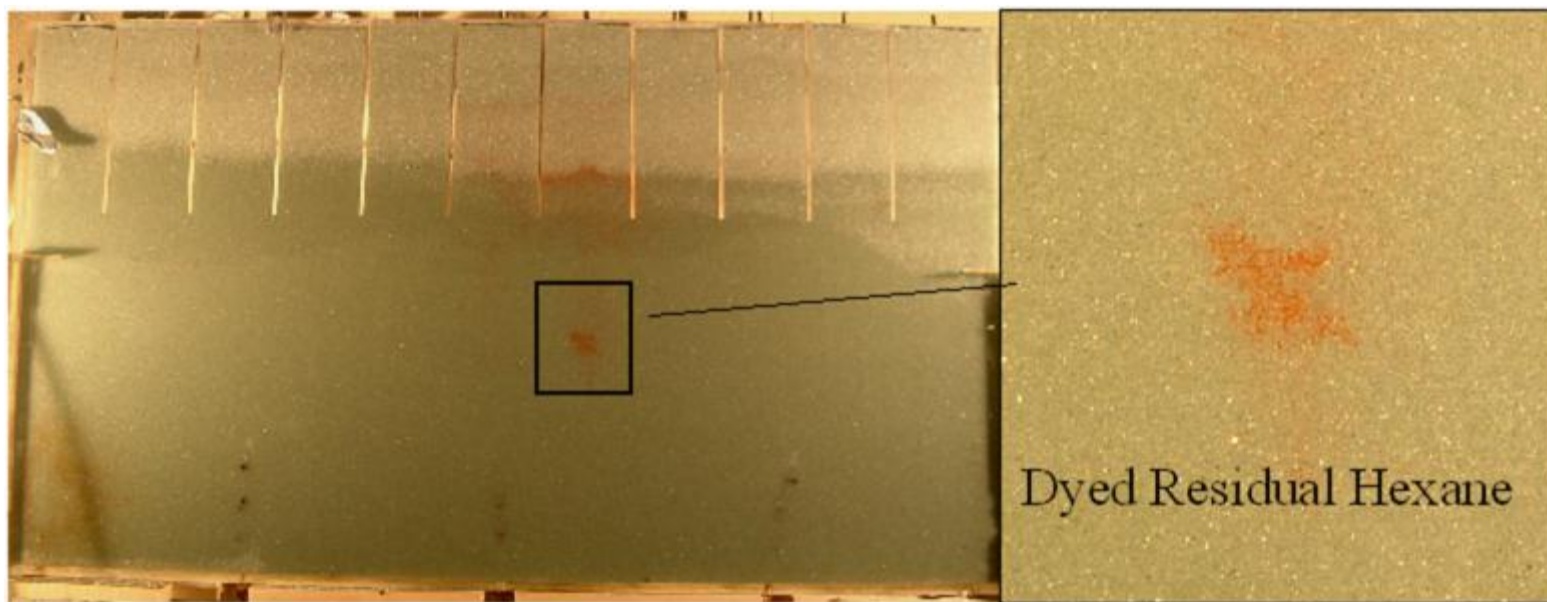
Proof of Concept in the Lab: *In Situ* Gas Saturation Development and Rate of Gas Ebullition



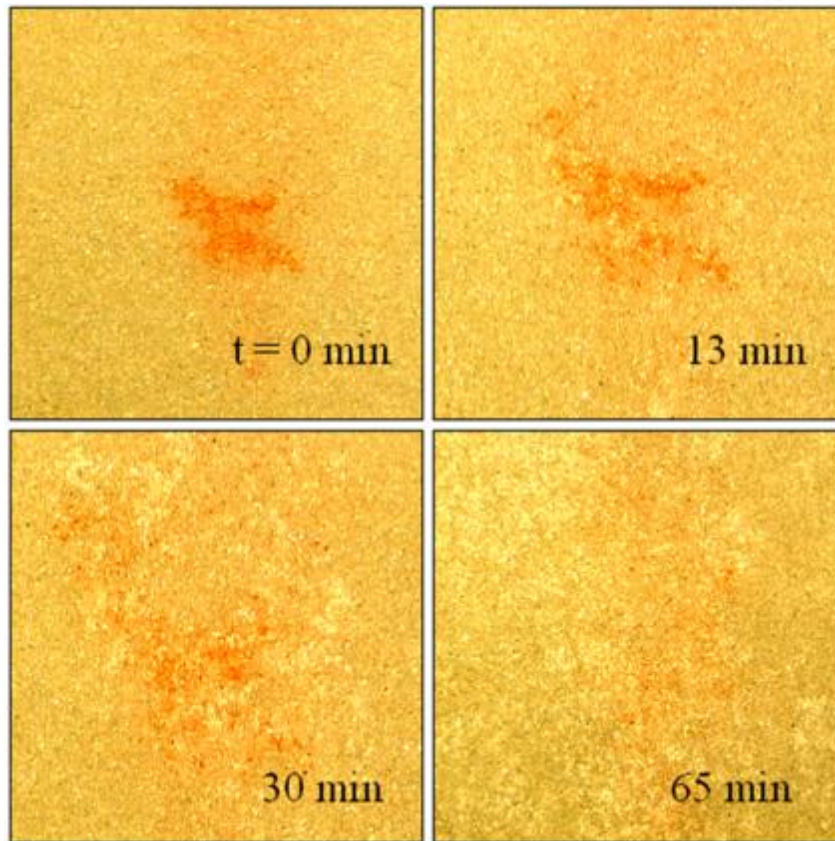
In Situ Gas Evolution



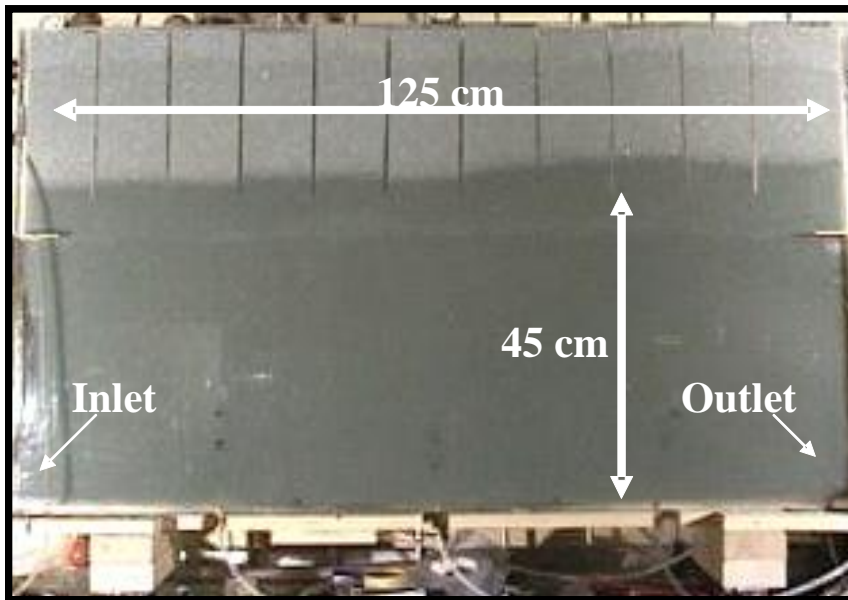
Recovery of Residual Hexane



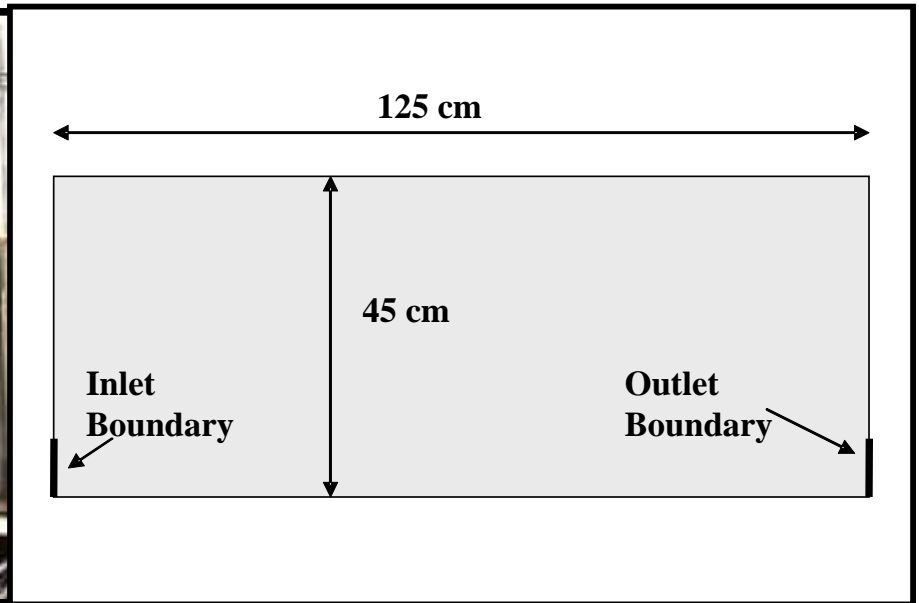
Recovery of Residual Hexane



Modeling of Lab Experiments



Experimental Apparatus

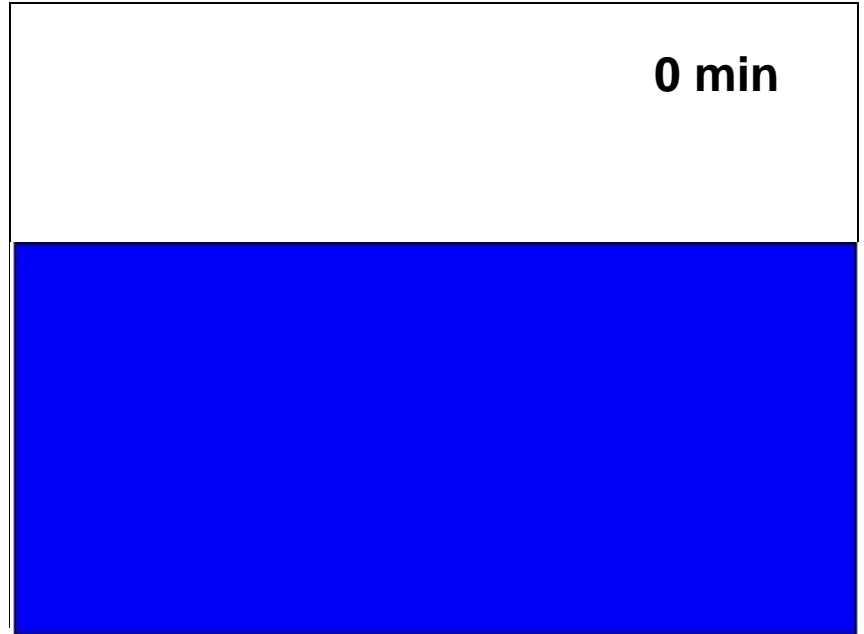
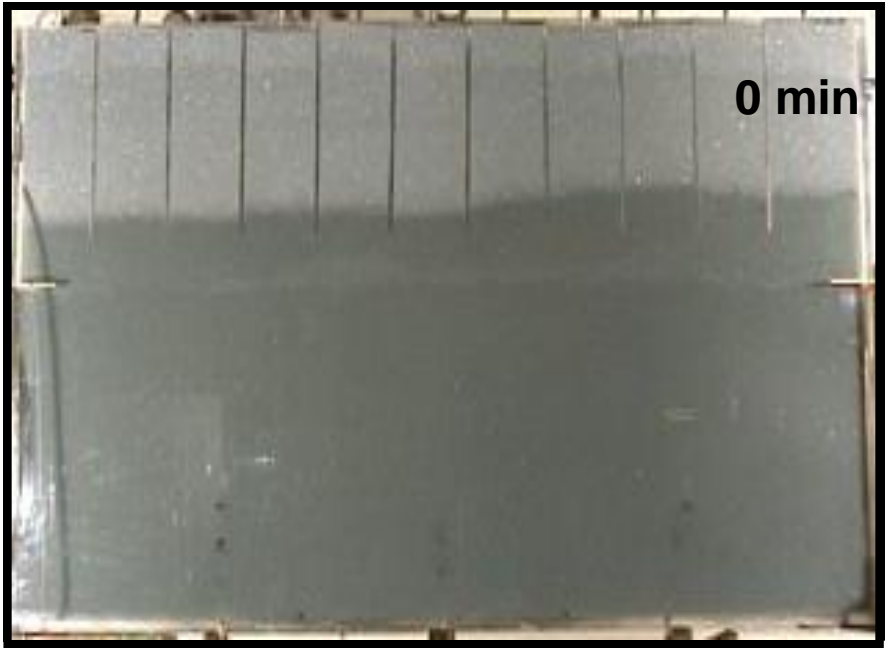


FEMLAB Simulation Domain



Comparison of Simulation to Experiment

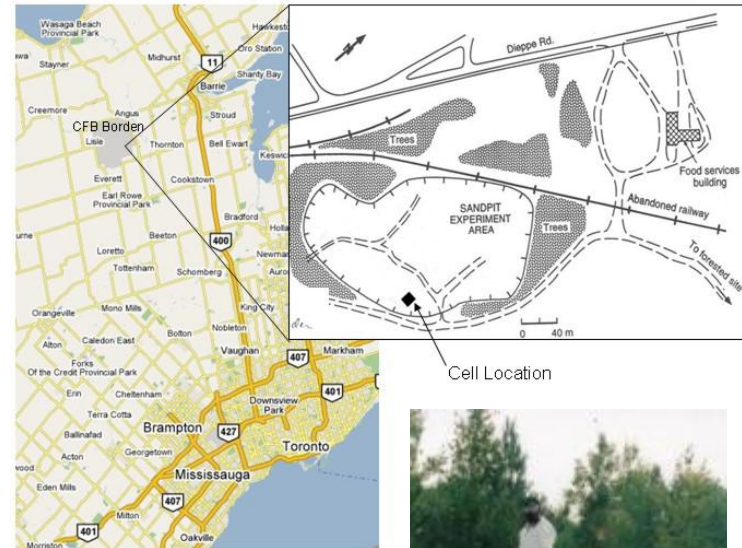
$$k_L\alpha = 0.01S_g \text{ s}^{-1}$$



$$v_{in} = 0.078 \text{ cm/s}, C_0 = 5.44 \text{ g/L}$$

Proof of Concept in the Field

- Enclosed cell at CFB Borden, Ontario
- 200 L of hydrocarbon mixture added to saturated zone
 - Pentane
 - Hexane
 - Soltrol



Nelson. *Field Trial of Residual LNAPL Recovery Using CO₂-Supersaturated Water Injection in the Borden Aquifer*, MS Thesis, University of Waterloo, 2007

tersusenv.com

Copyright © 2011 Tersus Environmental, LLC. All Rights Reserved.



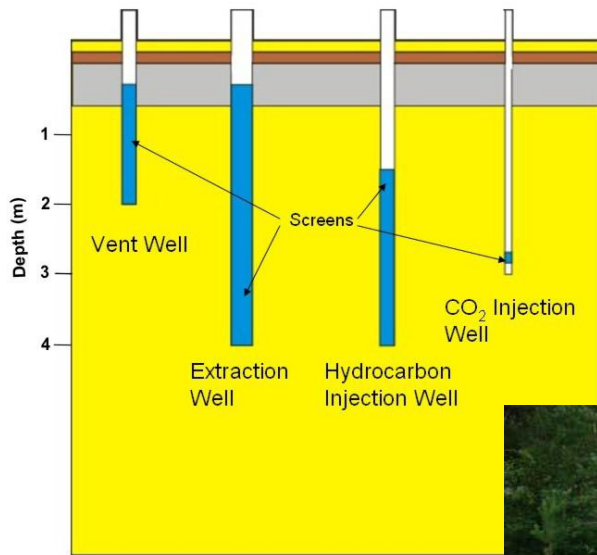
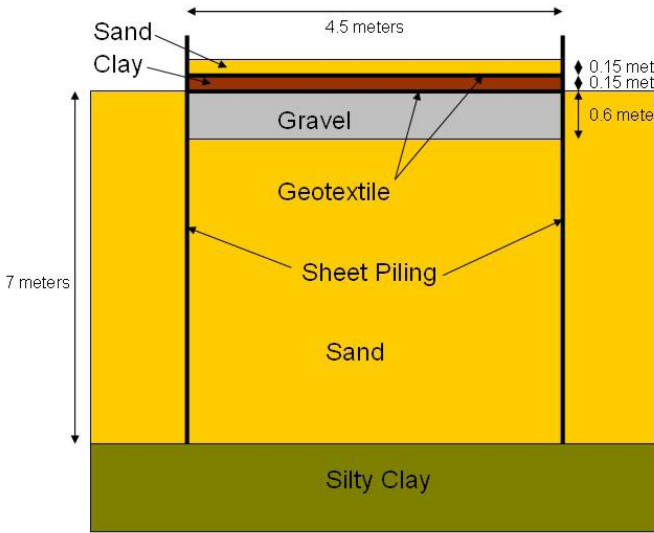
200 L Hydrocarbon Mixture



Nelson. Field Trial of Residual LNAPL Recovery Using CO₂-Supersaturated Water Injection in the Borden Aquifer, MS Thesis, University of Waterloo, 2007



The Test Cell



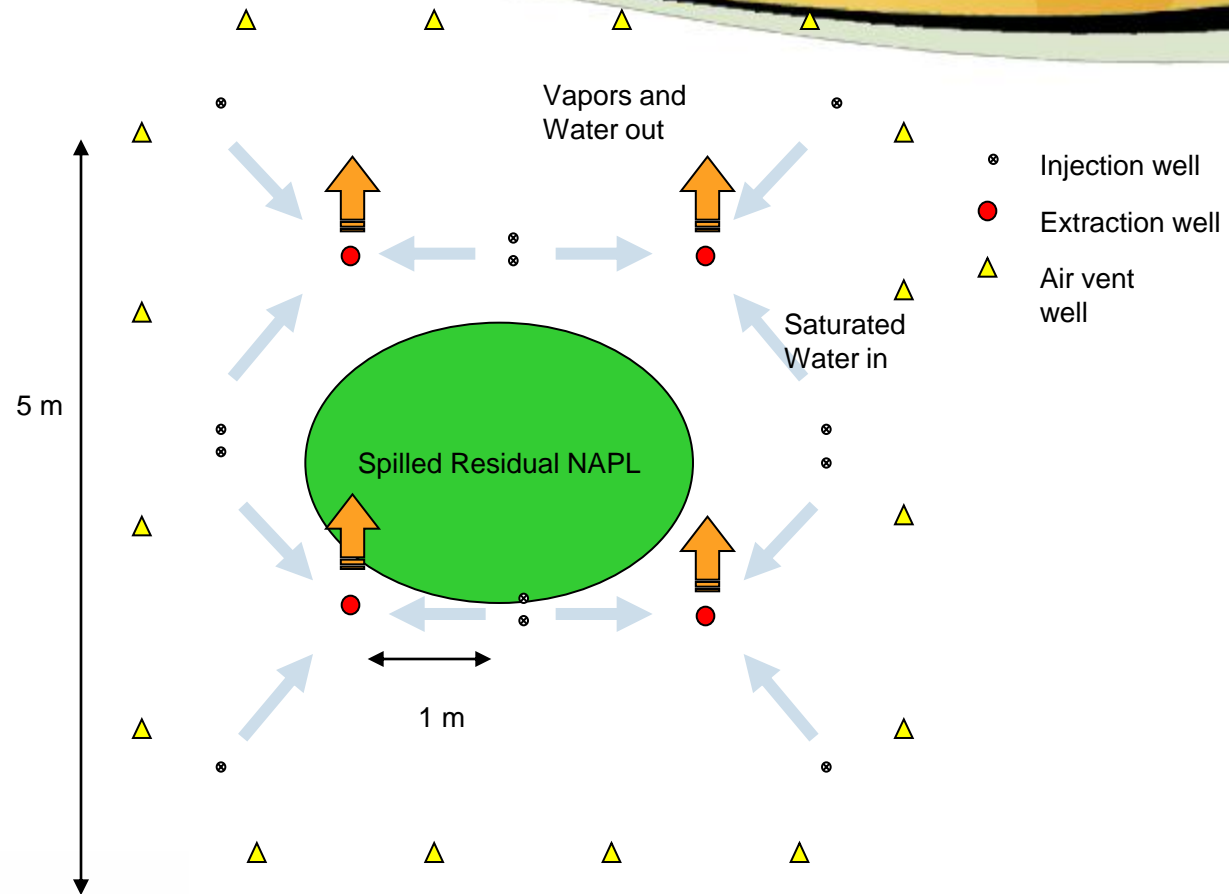
Nelson. *Field Trial of Residual LNAPL Recovery Using CO₂-Supersaturated Water Injection in the Borden Aquifer*, MS Thesis, University of Waterloo, 2007

tersusenv.com

Copyright © 2012 Tersus Environmental, LLC. All Rights Reserved.



Test Cell



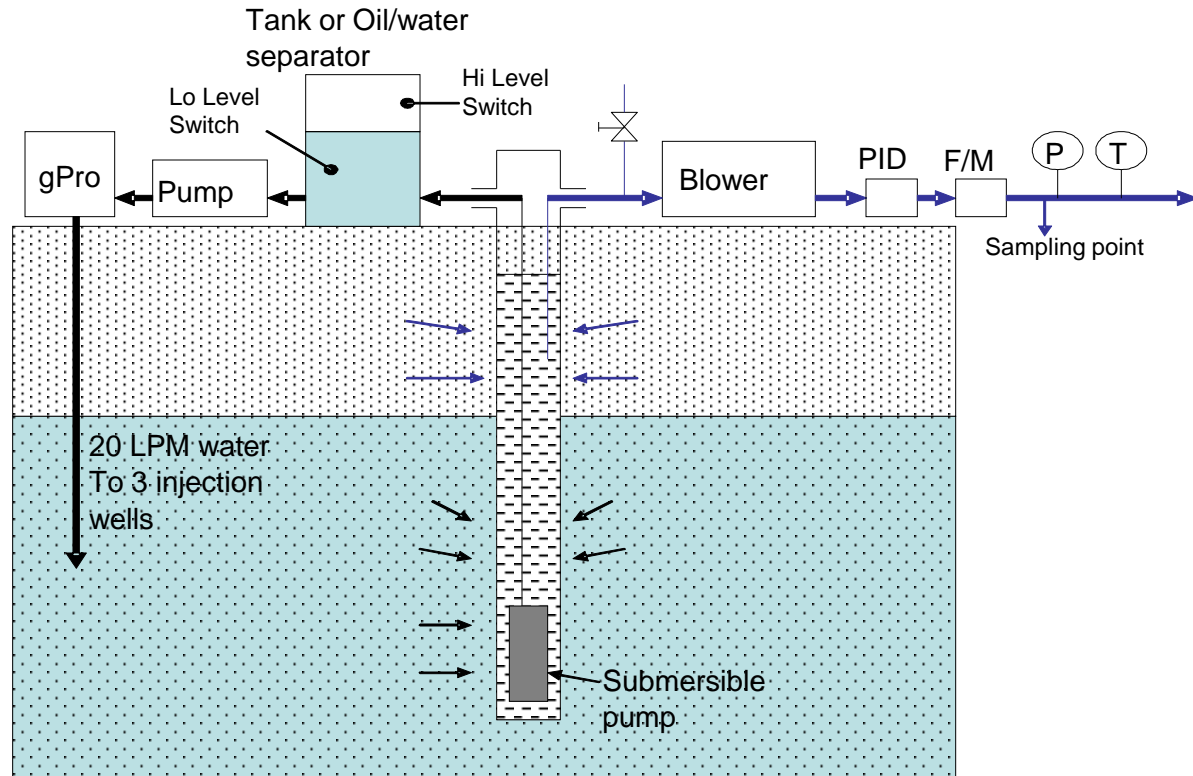
Nelson. *Field Trial of Residual LNAPL Recovery Using CO₂-Supersaturated Water Injection in the Borden Aquifer*, MS Thesis, University of Waterloo, 2007

tersusenv.com

Copyright © 2012 Tersus Environmental, LLC. All Rights Reserved.



SWI Field Experiment



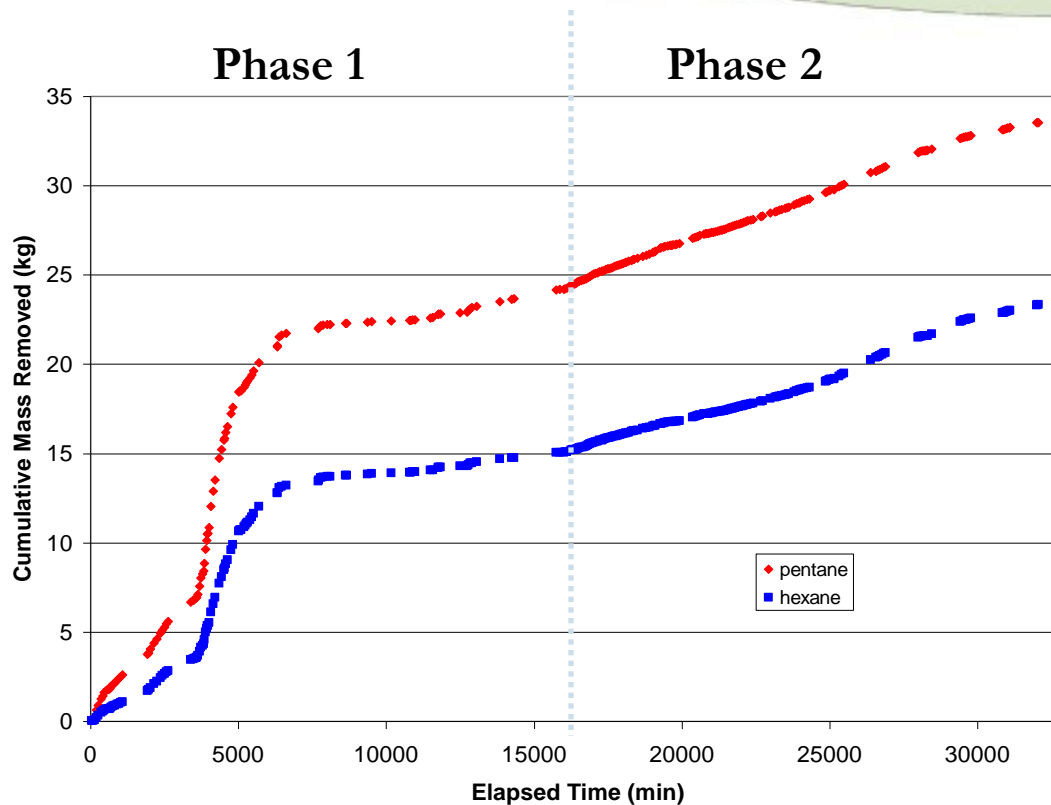
Nelson. *Field Trial of Residual LNAPL Recovery Using CO₂-Supersaturated Water Injection in the Borden Aquifer*, MS Thesis, University of Waterloo, 2007

tersusenv.com

Copyright © 2012 Tersus Environmental, LLC. All Rights Reserved.



SWI - NAPL Mass Removal



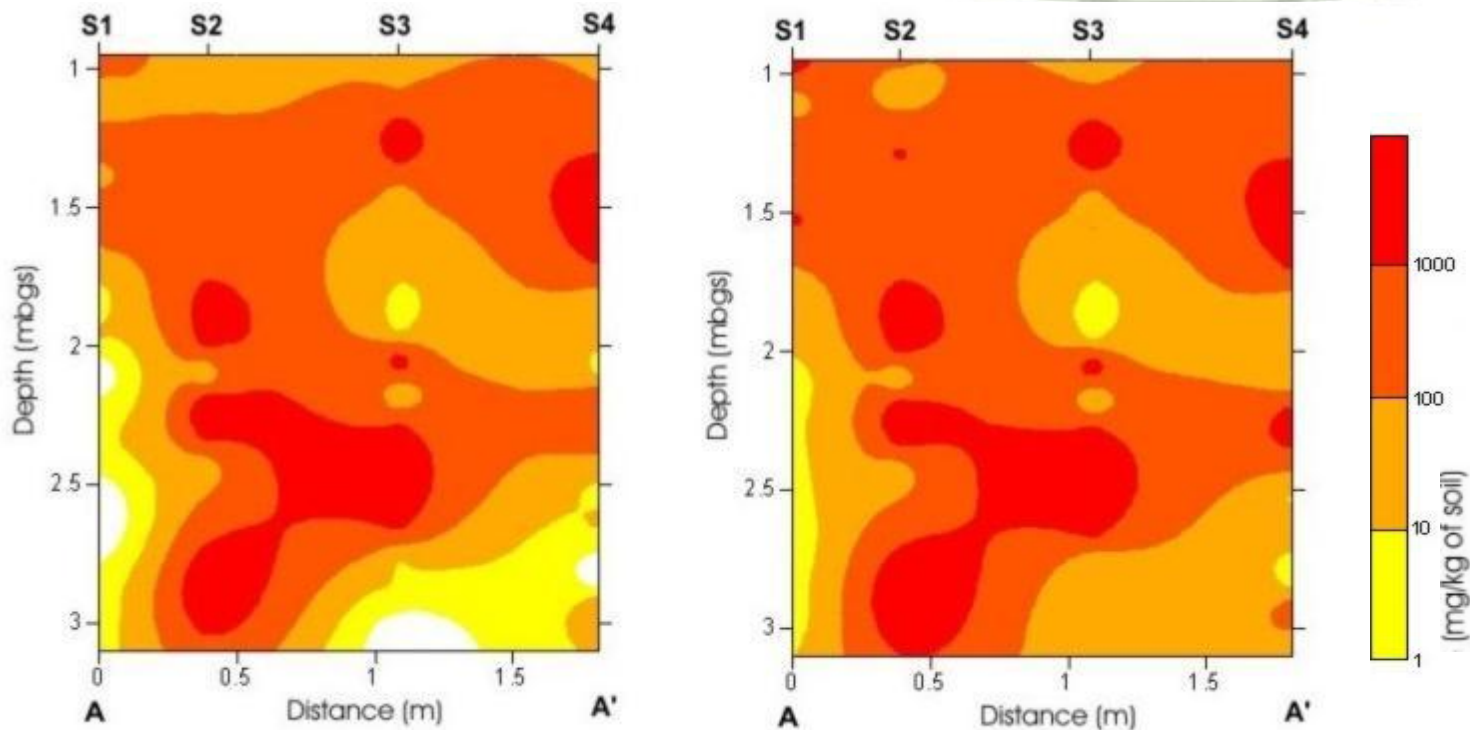
Nelson. *Field Trial of Residual LNAPL Recovery Using CO₂-Supersaturated Water Injection in the Borden Aquifer*, MS Thesis, University of Waterloo, 2007

tersusenv.com

Copyright © 2012 Tersus Environmental, LLC. All Rights Reserved.

Core Sampling- NAPL Concentration

Plane A (after 1st phase)



Pentane
(more volatile)

Hexane
(less volatile)

Nelson. *Field Trial of Residual LNAPL Recovery Using CO₂-Supersaturated Water Injection in the Borden Aquifer*, MS Thesis, University of Waterloo, 2007

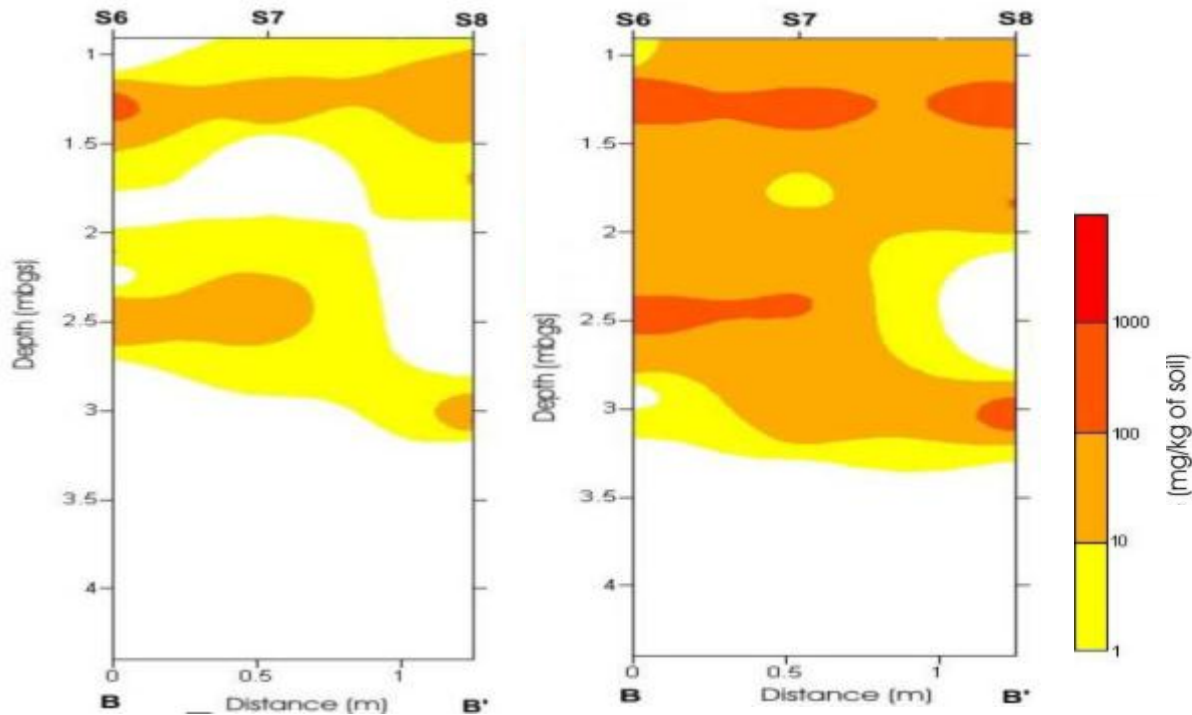
tersusenv.com

Copyright © 2012 Tersus Environmental, LLC. All Rights Reserved.



Core Sampling- NAPL Concentration

Plane B (after 2nd phase)



Pentane
(more volatile)

Hexane
(less volatile)

Nelson. *Field Trial of Residual LNAPL Recovery Using CO₂-Supersaturated Water Injection in the Borden Aquifer*, MS Thesis, University of Waterloo, 2007

tersusenv.com

Copyright © 2012 Tersus Environmental, LLC. All Rights Reserved.



NAPL Mass Removal

	Pentane		Hexane		Total	
	Mass (kg)	%	Mass (kg)	%	Mass (kg)	%
Phase I	24.2	57	15.1	35	39.3	44
Phase II	9.3	20	8.3	18	17.6	20
Total	33.5	77	23.3	53	56.8	64



Nelson. *Field Trial of Residual LNAPL Recovery Using CO₂-Supersaturated Water Injection in the Borden Aquifer*, MS Thesis, University of Waterloo, 2007

tersusenv.com

Copyright © 2012 Tersus Environmental, LLC. All Rights Reserved.



Demonstration Conclusions

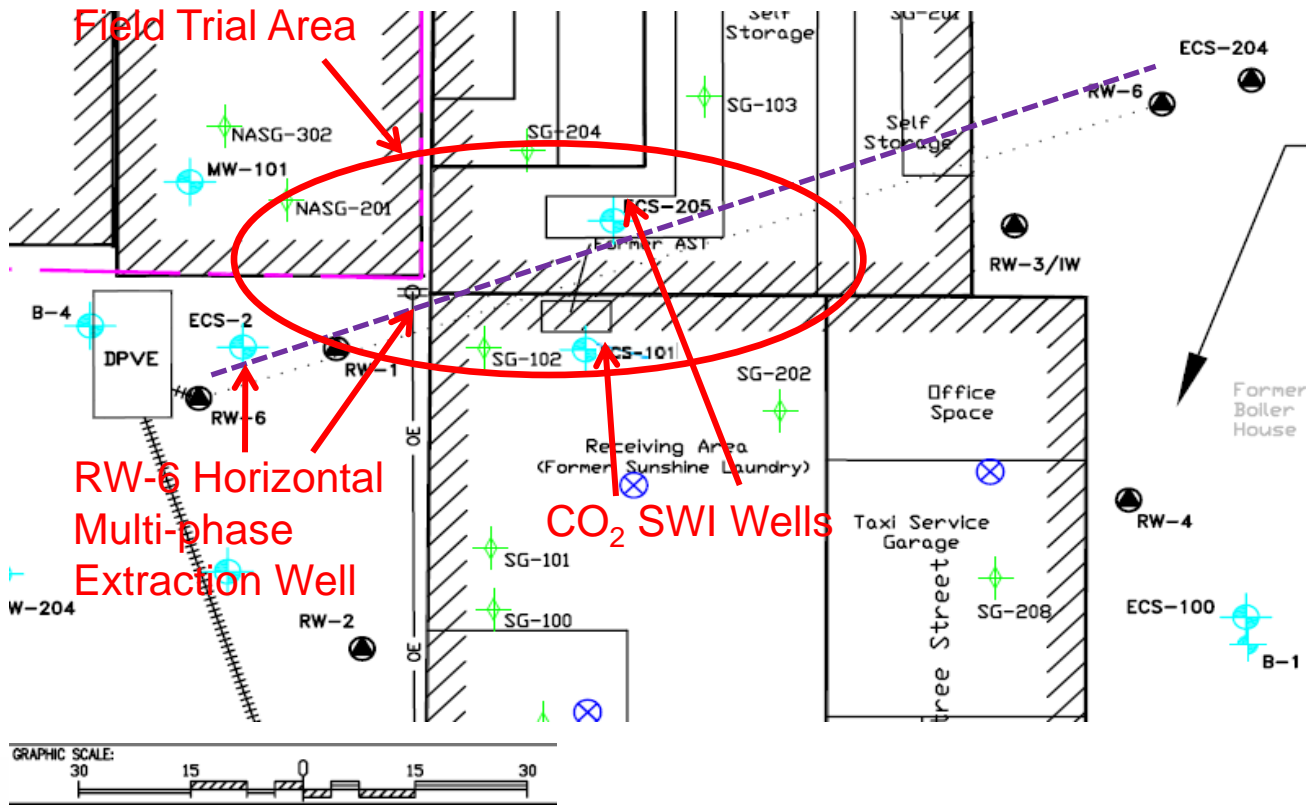
- Recovery by volatilization alone
 - 77 % of the Pentane
 - 53 % of the Hexane
- Majority of the NAPL mobilized towards water table
 - Available for liquid phase recovery



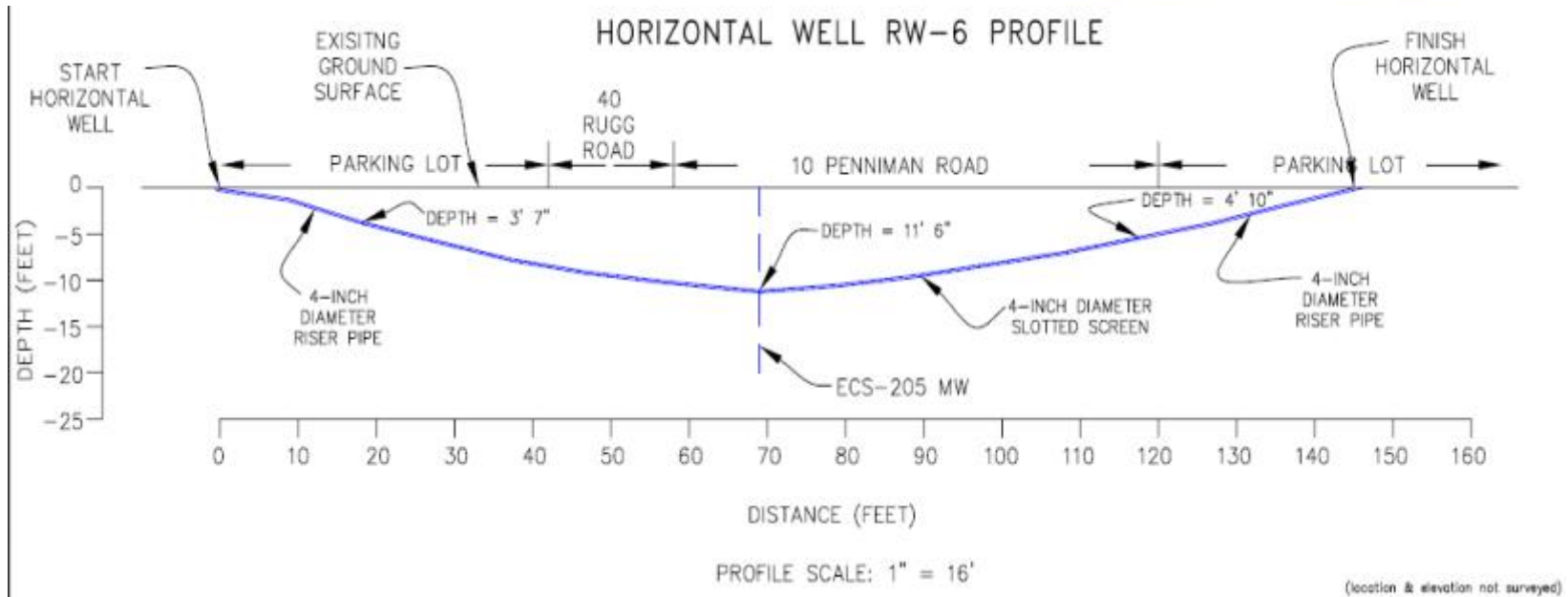


Boston PCE DNAPL CO₂ Saturated Water Injection Pilot

Well Layout



Extraction Well Profile



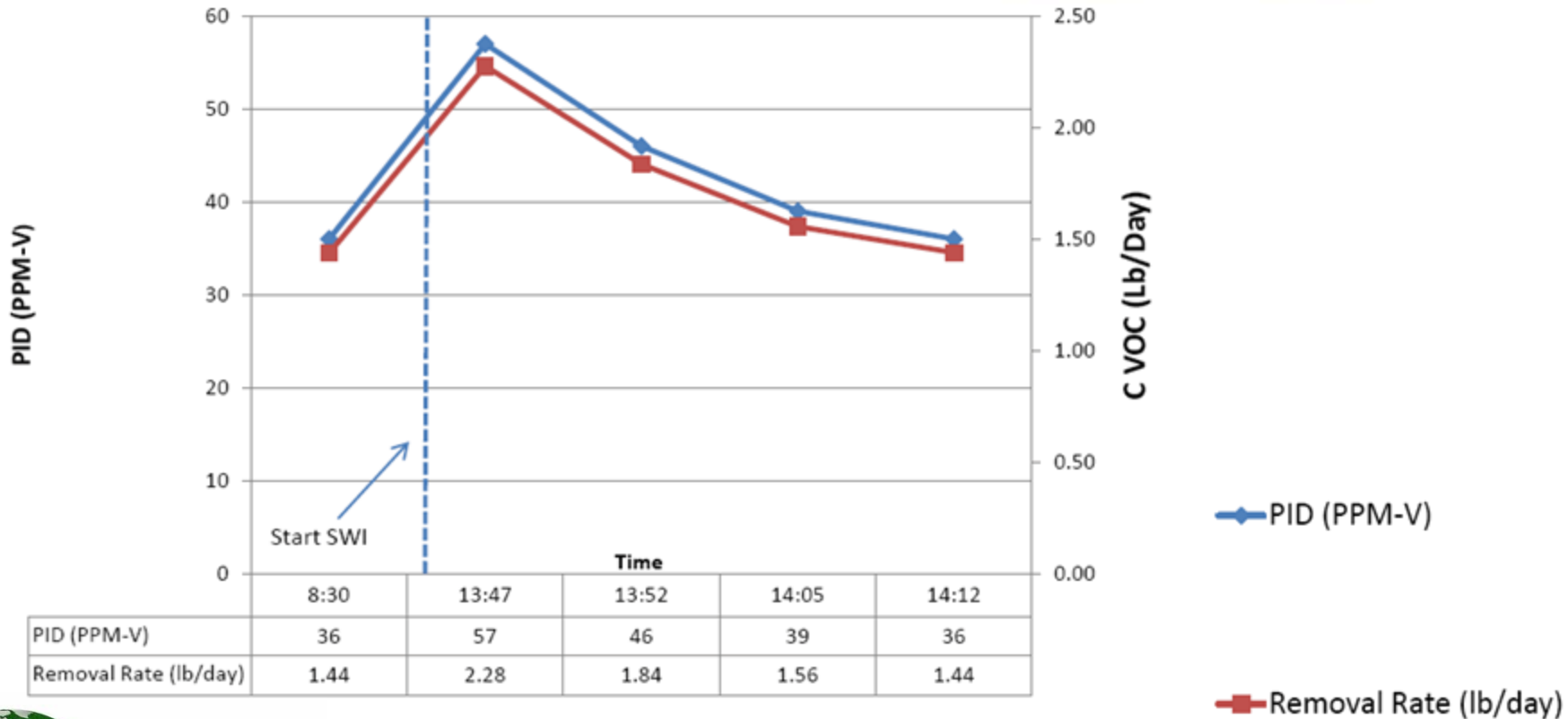
Notes:

Groundwater in silty sand formation

Depth to groundwater ~ 10 ft

Depth to impermeable clay ~16 to 20 ft

Extraction Rates (RW-6)



Injection Photos

gPRO Gas inFusion System



Carbonated Water Sample



Injection Well



CO₂ SWI Benefits

- SWI represents a significant improvement over unassisted dual phase extraction:
 - Greater zone of influence, recovery rate and percentage removed
 - NAPL trapped in pore space below the water table can be mobilized upwards by gas bubbles
 - Cost effective feasible implementation compatible with dual phase extraction



For More Information, Contact

Gary M. Birk, P.E.

Tersus Environmental

Tel: 307.638.2822 • Cell: 919.638.7892

Email: gary.birk@tersusenv.com

www.tersusenv.com



tersusenv.com

Copyright © 2011 Tersus Environmental, LLC. All Rights Reserved.

